AGU PUBLICATIONS

JGR

Journal of Geophysical Research: Solid Earth

RESEARCH ARTICLE
10.1002/2014JB011688

Key Points:
- Oceanic crust segregating to the CMB can form LLSVP-like thermochemical piles
- Mechanical stirring creates neutrally buoyant mix of dense and ambient materials
- LLSVPs interior is likely to be thermally and compositionally heterogeneous

Supporting Information:
- Texts S1 and S2 and Figure S1

Correspondence to:
E. Mulyukova,
mulyukova@gfz-potsdam.de

Citation:
Mulyukova, E., B. Steinberger, M. Dabrowski, and S. V. Sobolev (2015), Survival of LLSVPs for billions of years in a vigorously convecting mantle: Replenishment and destruction of chemical anomaly, *J. Geophys. Res. Solid Earth*, *120*, 3824–3847, doi:10.1002/2014JB011688.

Received 12 OCT 2014
Accepted 11 APR 2015
Accepted article online 15 APR 2015
Published online 21 May 2015

Survival of LLSVPs for billions of years in a vigorously convecting mantle: Replenishment and destruction of chemical anomaly

Elvira Mulyukova[1], Bernhard Steinberger[1,2], Marcin Dabrowski[3,4], and Stephan V. Sobolev[1,5]

[1]Physics of the Earth, GFZ German Research Center for Geosciences, Potsdam, Germany, [2]Centre for Earth Evolution and Dynamics, University of Oslo, Oslo, Norway, [3]Computational Geology Laboratory, Polish Geological Institute-National Research Institute, Wroclaw, Poland, [4]Physics of Geological Processes, University of Oslo, Oslo, Norway, [5]Institute of Earth and Environmental Science, University of Potsdam, Potsdam, Germany

Abstract We study segregation of the subducted oceanic crust (OC) at the core-mantle boundary and its ability to accumulate and form large thermochemical piles (such as the seismically observed Large Low Shear Velocity Provinces (LLSVPs)). Our high-resolution numerical simulations of thermochemical mantle convection suggest that the longevity of LLSVPs for up to three billion years, and possibly longer, can be ensured by a balance in the rate of segregation of high-density OC material to the core-mantle boundary (CMB) and the rate of its entrainment away from the CMB by mantle upwellings. For a range of parameters tested in this study, a large-scale compositional anomaly forms at the CMB, similar in shape and size to the LLSVPs. Neutrally buoyant thermochemical piles formed by mechanical stirring—where thermally induced negative density anomaly is balanced by the presence of a fraction of dense anomalous material—best resemble the geometry of LLSVPs. Such neutrally buoyant piles tend to emerge and survive for at least 3 Gyr in simulations with quite different parameters. We conclude that for a plausible range of values of density anomaly of OC material in the lower mantle—it is likely that it segregates to the CMB, gets mechanically mixed with the ambient material, and forms neutrally buoyant large-scale compositional anomalies similar in shape to the LLSVPs.

1. Introduction

One of the most robust results from deep seismic tomography studies is the existence of two antipodally located Large Low Shear Velocity Provinces (LLSVPs) at the base of the mantle: one beneath Africa and the other beneath the Pacific Ocean [*Garnero and McNamara*, 2008; *Dziewonski et al.*, 2010; *Ritsema et al.*, 2011]. These large-scale heterogeneities occupy ~1.6–2.4% of the total mantle volume [*Burke et al.*, 2008; *Hernlund and Houser*, 2008] and appear to be stable in their positions, long-lived, and affect the geometry of flow in the deep mantle and that of plate tectonics at the surface [*Dziewonski et al.*, 2010]. In particular, plumes of arguably deep origin, manifested at the surface as eruption sites of large igneous provinces, hot spot volcanoes, and kimberlites, are thought to be generated from the margins of the LLSVPs [*Torsvik et al.*, 2006].

The negative correlation between the bulk sound and shear velocity within the LLSVPs suggests that these anomalies are of chemical origin [*Masters et al.*, 2000; *Trampert et al.*, 2004; *Steinberger and Holme*, 2008]. This hypothesis is supported by the normal-mode data, which indicate an increased density in the locations of LLSVPs [*Ishii and Tromp*, 1999]. Further, seismic data in conjunction with available mineral physics data reveal the dominant role of chemically induced density variations in the lowermost 1000 km of the mantle [*Trampert et al.*, 2004; *Mosca et al.*, 2012]. The sharp and steeply dipping edges of the African LLSVP are also best explained as compositionally controlled [*Ni et al.*, 2002].

Although there is substantial evidence for the compositionally anomalous nature of the LLSVPs, there is yet no consensus on the origin of their constituting dense material. Suggestions from previous studies fall within three categories: (i) a primordial layer that formed early in the Earth's history [e.g., *Labrosse et al.*, 2007; *Lee et al.*, 2010], (ii) accumulation of a dense eclogitic component from the subducted oceanic crust that segregates at the core-mantle boundary (CMB) [*Hofmann and White*, 1982; *Christensen and Hofmann*, 1994; *Tackley*, 2011], and (iii) outer core material leaking into the lower mantle [*Hayden and Watson*, 2007]. In this study, we explore the feasibility, from a geodynamic point of view, of scenario (ii).

Oceanic crust (OC) enters the lower mantle through deeply penetrating subducting slabs [*Van der Hilst et al.*, 1998] — a process that has been taking place for 3–4 billion years [*Nutman*, 2006; *Shirey and Richardson*, 2011]. The amount of OC that has been produced over this period of time (which itself is uncertain by ~1 Gyr) shows that 7–53% of the mantle volume today may be occupied by mid-ocean ridge basalt (MORB) material [*Xie and Tackley*, 2004; *Stixrude and Lithgow-Bertelloni*, 2012], which is more than sufficient to make up the total volume of the LLSVPs.

Intrinsic density of the subducted OC may be 0.5–5.3% higher than that of the ambient lower mantle [e.g., *Hirose et al.*, 2005; *Ricolleau et al.*, 2010]. This has given rise to the hypothesis that the high-density basaltic OC component may segregate and accumulate at the CMB and occasionally get sampled and brought back to the surface by deep mantle plumes. There also exists geochemical evidence to support this notion: *Hofmann and White* [1982] proposed that recycling of previously subducted OC into plumes may explain some of the observed difference in geochemical signature between ocean island basalt and MORB. Studies of olivines from the Hawaiian lavas [*Kobayashi et al.*, 2004; *Sobolev et al.*, 2005], the Siberian Flood Basalts [*Sobolev et al.*, 2011], and other plumes [*Sobolev et al.*, 2007] reveal contribution of the recycled OC to the observed geochemical heterogeneity.

1.1. Previous Models

Some of the uncertainty associated with the origin of LLSVPs derives from the lack of understanding of mantle evolution, which in turn stems from the uncertainty of its constituting materials and their physical properties. Geodynamic studies of thermochemical mantle convection typically attempt to find the range of material properties that allows generation and/or sustainability of high-topography thermochemical piles at the base of the mantle, which are laterally stable, manage to survive billions of years of entrainment by ambient flow, and have hot thermal plumes generated predominantly at their edges [e.g., *Tan et al.*, 2011; *Bower et al.*, 2013; *Li et al.*, 2014].

In general, results of numerical and experimental studies indicate that chemically distinct material with an intrinsic density elevated by a few percent can form piles that can be maintained in the deeper mantle for billions of years, with thermally or compositionally induced viscosity variations promoting the long-term stability [e.g., *Kellogg et al.*, 1999; *Davaille*, 1999; *Davaille et al.*, 2002; *Tackley*, 2002; *Zhong and Hager*, 2003]. In order to satisfy both long-term survival and geometrical (e.g., topography) constraints of the LLSVPs, their thermal and compositional buoyancies must be roughly balanced [*Garnero and McNamara*, 2008]. High-topography and gravitationally stable thermochemical piles, with plumes forming predominantly at their edges, were obtained in numerical models of *Tan et al.* [2011] and *Li et al.* [2014]. Success of their models to reproduce these observational constraints was attributed to the depth dependence of the compositional density anomaly (i.e., decreasing with depth), with a moderate value of the compositional density anomaly at the CMB (~1.6–2.9% of the ambient mantle density) and large thermally induced viscosity variations ($> 10^4$).

Early numerical models of segregation of subducted OC, using an isoviscous model of the mantle, found that with a compositional density contrast below 5%, it is unlikely for significant segregation and accumulation at the CMB to occur [*Gurnis*, 1986]. However, despite resistance to segregation, clumps of OC material can persist in the mantle for a few billion years, thanks to the inefficiency of stirring by large-scale mantle flow [*Gurnis and Davies*, 1986a]. The convective mixing is even less efficient when the depth dependence of viscosity is introduced [*Gurnis and Davies*, 1986b]. Using a more realistic model of the mantle, which incorporates both temperature dependence and depth dependence of viscosity, *Christensen and Hofmann* [1994] showed that if the OC reaches the bottom thermal boundary layer, where the viscosity is lowered due to high temperature, it may segregate from the rest of the lithosphere and accumulate at the bottom. This result is in agreement with three-dimensional modeling studies of segregating slabs [*Tackley*, 2011].

In general, results from numerical models suggest that segregation of OC and its persistence at the bottom are enhanced for larger values of compositional density anomaly [*Gurnis*, 1986; *Christensen and Hofmann*, 1994; *Davies*, 2002; *Nakagawa and Tackley*, 2005; *Brandenburg and Van Keken*, 2007; *Huang and Davies*, 2007; *Nakagawa et al.*, 2010; *Li and McNamara*, 2013; *Nakagawa and Tackley*, 2014]. Increasing temperature dependence of viscosity was found to significantly promote segregation in models of *Christensen and Hofmann* [1994], but the opposite was suggested by the numerical results of *Li and McNamara* [2013]. It is worth noting that in no cases studied by *Li and McNamara* [2013] did significant segregation of OC occur. The numerical study of *Nakagawa and Tackley* [2014] suggests that the Rayleigh number (*Ra* — a nondimensional parameter describing vigor of convection) plays a more dominant role in accumulation of OC at the CMB than thermally

induced viscosity variations. In contrast to *Christensen and Hofmann* [1994] and *Li and McNamara* [2013], who also looked at the effect of *Ra*, *Nakagawa and Tackley* [2014] found that increasing *Ra* enhances pile formation by segregated OC. Thus, the effect of viscosity variations in the deep mantle (which also influence the value of *Ra*) on formation of a large-scale compositional heterogeneity over time remains unclear.

1.2. This Study

In models where thermochemical piles are generated by segregation and accumulation of dense OC, the interior structure of the piles and their large-scale characteristics (shape, volume, and buoyancy with respect to ambient mantle) are determined by processes that may be highly variable in time: rate of segregation of dense material at the CMB, rate of its reentrainment by plumes, and stirring taking place in the interior of the piles. Thus, the bulk properties of the piles cannot be straighforwardly prescribed as part of the initial conditions (as is the case with models featuring piles generated by deforming an initially flat dense basal layer), but emerge self-consistently as part of the simulation result.

Here we present the results of thermochemical convection simulations that illustrate the dynamics and thermal and compositional evolution of large-scale compositional heterogeneities at the CMB, which develop self-consistently by segregation and accumulation of subducted OC. Guided by the results from previous studies, we use a thin (6 km) OC, to conservatively estimate its perturbation to the ambient flow and settling at the CMB, and a rheological model of the mantle that leads to realistically large thermally induced viscosity variations.

2. Model Description

2.1. Mathematical Formulation

We model thermochemical convection of a Boussinesq fluid at infinite Prandtl number in a two-dimensional hollow cylinder geometry. Equations that describe the dynamics of the flow are the conservation equations of momentum, mass, energy, and composition presented in their nondimensional form:

$$-\frac{\partial p}{\partial x_i}+\frac{\partial \tau_{ji}}{\partial x_j}=Ra\,(T+BrC)\,g_i \tag{1}$$

$$\frac{\partial v_i}{\partial x_i}=0 \tag{2}$$

$$\frac{\mathrm{D}T}{\mathrm{D}t}=\frac{\partial}{\partial x_i}\left(\frac{\partial T}{\partial x_i}\right) \tag{3}$$

$$\frac{\mathrm{D}C}{\mathrm{D}t}=0 \tag{4}$$

where we used the standard transformation of variables for nondimensionalization, e.g., as in *Schubert et al.* [2001]. The reference values of the physical parameters used for nondimensionalization are presented in Table 1. In equation (3), the source term is omitted (i.e., set to zero), since our models do not have any internal heating (see section A4 for the effects of excluding internal heating on our results). Subscripts i and j denote the Cartesian components of vector and tensor quantities, x_i is the position vector, v_i the velocity vector, p the deviation of pressure from its reference state, τ_{ij} the deviatoric stress tensor, g_i the unit vector in the direction of gravity, T the deviation of dimensionless temperature from its surface value ($T=0$ translates to temperature at the surface (285 K), $T=1$ to temperature at the CMB (3500 K), and $T=0.5$ to reference adiabatic temperature (~1890 K)), t is time, and $\frac{\mathrm{D}}{\mathrm{D}t}$ is the material derivative. *Ra* is the Rayleigh number, which describes the vigor of convection and is defined as the ratio between the buoyancy forces driving convection and the dissipative effects opposing convection:

$$Ra\equiv\frac{\alpha_r' g_r' \rho_r' \triangle T_r' D_r'^3}{\kappa_r' \eta_r'}\approx 1.5\cdot 10^7 \tag{5}$$

where the *Ra* value was obtained according to the values presented in Table 1 (primes denote dimensional quantities). The *Ra* number used in our study is comparable to the ones used in similar, previously published studies: e.g., $Ra=[2.5\cdot 10^5-1\cdot 10^6]$ in *Christensen* [1984], $Ra=[1\cdot 10^6-1\cdot 10^7]$ in *Brandenburg and Van Keken* [2007], $Ra=1\cdot 10^7$ in *Nakagawa and Tackley* [2005] and *Nakagawa et al.* [2010], $Ra=[5\cdot 10^6-5\cdot 10^7]$ in *Li and McNamara* [2013], and $Ra=[1\cdot 10^7-1\cdot 10^8]$ in *Nakagawa and Tackley* [2014].

Table 1. Physical and Geometrical Parameters Representative of the Earth's Deep Mantle [e.g., *Dziewonski and Anderson*, 1981; *Schubert et al.*, 2001; *Steinberger and Calderwood*, 2006; *Tackley*, 2012], Which We Use for Nondimensionalization[a]

Quantity	Symbol	Values Representative of Deep Mantle	Units
Gravitational acceleration	g'_r	10	m s^{-2}
Thermal expansivity	α'_r	$1 \cdot 10^{-5}$	K^{-1}
Density	ρ'_r	$5.5 \cdot 10^{3}$	kg m^{-3}
Temperature drop across mantle depth	$\triangle T'_r$	3215	K
Depth of the mantle	D'_r	$2.9 \cdot 10^{6}$	m
Thermal diffusivity	κ'_r	$6 \cdot 10^{-7}$	m^2 s^{-1}
Dynamic viscosity	η'_r	$5 \cdot 10^{21}$	Pa s
Specific heat capacity	c'_{p_r}	1250	kJ kg^{-1} K^{-1}

[a]Prime denotes dimensional quantity, and subscript *r* denotes reference quantities.

Br is the buoyancy ratio, which describes the relative strength of the compositionally and thermally induced density variations:

$$Br \equiv \frac{\triangle \rho'_C}{\alpha'_r \rho'_r \triangle T'_r} \tag{6}$$

where $\triangle \rho'_C$ stands for the compositionally induced density variations. In our simulations, *Br* is systematically varied from ~0.57 to ~1.1 (corresponding to 1.8% and 3.6% compositional density anomaly, respectively).

In equation (4), $C(\vec{x})$ describes spatial distribution of different materials (phases). In the presented work, we only consider immiscible fluids and disregard cases of chemical mixtures of different materials. Thus, $C(\vec{x})$ is a discrete indicator function that can assume values 0 or 1 (since we only have two phases): $C(\vec{x})$=1 if $\vec{x}$ is occupied by the compositionally dense material and $C(\vec{x}) = 0$ otherwise.

We model materials constituting the Earth's mantle as fluids whose rate of deformation $\dot{\epsilon}_{ij}$ and deviatoric stress τ_{ij} are linearly dependent (Newtonian fluids). We also assume them to be incompressible and isotropic. In this case, the deviatoric stress, which appears in equation (1), can be expressed in terms of rate of deformation—and thus velocity, using the following constitutive relation:

$$\tau_{ij} = 2\eta\dot{\epsilon}_{ij} = \eta\left(\frac{\partial v_i}{\partial x_j} + \frac{\partial v_j}{\partial x_i}\right) \tag{7}$$

Assuming incompressibilily of the mantle across its depth is not a fully justified approximation for mantle-like thickness and material properties [e.g., *Schubert et al.*, 2001]. Some of the consequences of adopting it in our model, most important of which are the lack of the associated pressure dependencies of various material properties (e.g., density and thermal expansivity), are outlined in section A1.

2.2. Boundary and Initial Conditions

To close the system of equations (1)–(7), mechanical (velocity or traction) and thermal (temperature or heat flux) boundary conditions must be provided, together with the initial conditions for temperature and composition. Mechanical boundary conditions used in our models are free slip and impermeable at the inner boundary of the cylinder and prescribed velocities at the outer boundary. The tangential component of the prescribed surface velocity V'_s is a sinusoidal function of azimuthal position θ along the outer boundary: $V'_s = A_{V_s}\sin(2\theta)$, with the amplitude $A_{V_s} = 1$ cm/yr. The schematic of the prescribed velocity boundary condition is given in Figure 1. The prescribed surface velocity in our models is somewhat lower than what is representative for the tectonic plate velocities. This is because the role of the prescribed surface velocity in our model is mainly to organize the flow such as to form two downwelling regions. As was shown in the analogue experiments of *Gonnermann et al.* [2004], increasing the magnitude of the surface velocity suppresses the naturally developing convecting pattern, which we try to avoid in our models. See section A3 for the discussion about the effects of prescribed velocity on our modeling results.

Thermal boundary conditions constitute prescribed temperatures at both inner (T=1) and outer (T= 0) boundaries. For initial temperature conditions, we use results of a convection model with the same geometry

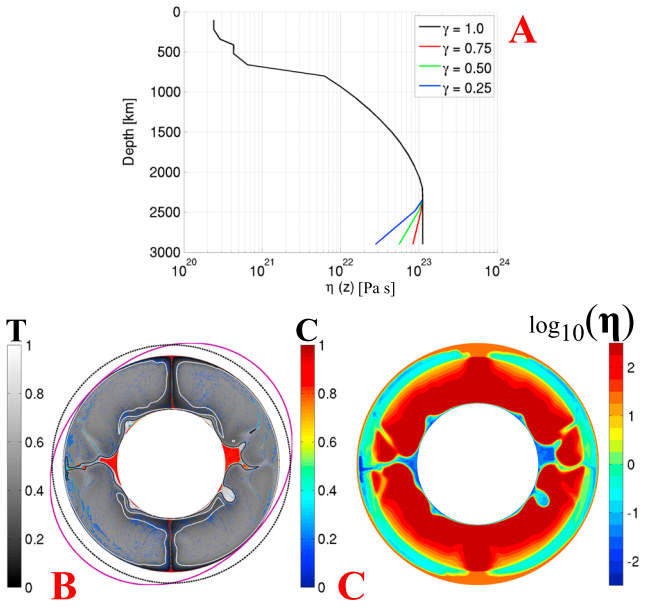

Figure 1. (a) Optimized radial viscosity profile, modified from *Steinberger and Calderwood* [2006] to exclude the effect of thermal boundary layers. The colored lines indicate the effect on viscosity of different values of γ—a variable that we use to lower the viscosity in the bottommost 500 km of the domain, according to legend (see section 2.3 for details). (b) Snapshot from one of the simulations to explain the setup of numerical experiments. The gray-scale color field represents the nondimensional thermal field (color bar on the left). Red-blue color scale represents the fraction of OC material (color bar in the center). Regions where OC fraction is less than 0.1 are made transparent. The black and white lines are hot ($T = 0.6$) and cold ($T = 0.3$) isotherms, respectively. The purple line on the exterior illustrates the direction of the tangential component of the imposed surface velocity V_s' (negative means clockwise)—black dashed line indicates the zero value. V_s' is a function of azimuthal position θ: $V_s' = A_{V_s} \sin(2\theta)$, where $A_{V_s} = 1$ cm/yr. (c) Same snapshot as in Figure 1b but showing decadic logarithm of nondimensional viscosity (color bar on the right).

as in our tested models but at a coarser resolution, without any compositional heterogeneities and which was simulated for 500 Myr (starting with $T = 0$ at the surface, $T = 1$ at the CMB, and $T = 0.5$ everywhere else). The initial temperature field used for the models is such that the net surface heat flow is larger than the net bottom heat flow, and thus, the system starts off with mantle cooling. Over the last gigayear of simulation time, our results show mantle cooling at a rate of 10.5–14.5 TW (when dimensionalized modeled heat flux is averaged over 2-D surfaces and integrated over the real Earth's 3-D surfaces) for different tested cases, which is partially due to their initial thermal conditions and partially due to their developing dense basal structures.

Melting of the shallow mantle which forms basaltic oceanic crust (OC) is modeled in a simplified way, analogous to models of *Christensen and Hofmann* [1994] and *Li and McNamara* [2013]: material that enters the top 6 km of the cylindrical domain (so-called "melting zone") is converted to OC, which is intrinsically denser than the ambient material (if the material happens to be OC prior to entering the "melting zone," it remains unchanged). In this way, the compositional anomaly is continuously generated throughout the simulation.

The nondimensional inner and outer radii of our cylindrical domain are set to 1 and 2, respectively. It is an intermediate scaling compared to the ones studied in *van Keken* [2001]. See section A2 for the discussion on how this choice of geometry affects our results and how it compares to geometries used in other numerical studies.

2.3. Rheological Model

The rheological model used in this study includes depth dependence and temperature dependence of viscosity [*Steinberger and Calderwood*, 2006]. Variation of viscosity with depth is illustrated in Figure 1, evaluated at mean temperature value (i.e., nondimensional value of $T = 0.5$). Temperature variations that arise in the course of simulations alter this profile, according to the following relations:

$$\eta = \eta(z) \cdot \exp\left(-\frac{H}{nR\bar{T}} \frac{T - T_{\text{off}}}{(T - T_{\text{off}} + \frac{\bar{T}}{T_{\text{scale}}})}\right) \tag{8}$$

$$T_{\text{scale}} = T_{\text{CMB}} - T_0 - \triangle\bar{T} \approx 2348K$$

$$T_{\text{off}} = \frac{\bar{T}_0 - T_0}{T_{\text{scale}}} \approx 0.5658$$

where $\eta(z)$ is the reference viscosity profile at adiabatic temperature (see Text S1 in the supporting information for derivation of $\eta(z)$), H the activation enthalpy, n the stress exponent ($n = 3.5$ above 660 km depth, and

n=1 below 660 km depth), $\bar{T}(z)$ the adiabatic reference temperature profile (note that $\bar{T}(z)$ is different from the reference temperature profile used in the linearization of the conservation equations, with the latter simply being a constant due to the Boussinesq approximation), T are the nondimensional temperature values computed in the course of the simulation, $T_{CMB} = 3500$ K and $T_0 = 285$ K are the assumed temperature values at the core-mantle boundary and at the surface, respectively, and $\triangle\bar{T} \approx 866$ K is the adiabatic temperature increase across the depth of the mantle. The offset temperature T_{off} and the scaling temperature T_{scale} are used in order to correct for the fact that different reference temperature profiles are used in the general (Boussinesq) model, according to which T is computed, and in the viscosity model, where $\bar{T}$ and δT are used. We use cutoff values 10^{19} and 10^{24} Pa s—to restrict viscosity variations to the respective range. The viscosity field obtained in a typical run of thermochemical convection simulation is presented in Figure 1. See Text S1 in the supporting information for details of derivation and values of the physical parameters used in the rheological model.

Dependence of viscosity on depth, temperature, and composition have all been shown to play an important role in determining the rate of entrainment upward and segregation to the bottom of an intrinsically dense compositional anomaly [e.g., *Gurnis*, 1986; *Gurnis and Davies*, 1986b; *Sleep*, 1988; *Solomatov et al.*, 1993; *Davaille*, 1999; *Zhong and Hager*, 2003; *Lin and van Keken*, 2006; *Kumagai et al.*, 2007; *Li and McNamara*, 2013]. Unfortunately, observational and experimental data on viscosity variation and value in the deep lower mantle (within and above the thermal boundary layer overlying CMB) are uncertain to ~1 order of magnitude (see *Tackley* [2012] for a recent overview). Temperature, composition (i.e., presence of postperovskite phase, or distribution of the two main phases—perovskite and magnesiowustite), grain size, deformation history, and creep mechanism (possible occurrence of dislocation creep in regions of high stress, rather than the commonly assumed diffusion creep) in the lowermost mantle may all have a say on its effective viscosity.

In our models, viscosity model is varied only in the lowermost 500 km of the mantle. We do not attribute its variation to any specific mechanism outlined above. Rather, we treat it as an uncertainty in the lowermost part of the radial viscosity profile, shown by the black line in Figure 1, which is varied for different models to investigate the effect of this uncertainty. We define a parameter γ as follows:

$$\gamma = \frac{\eta_{red}}{\eta_{orig}} \tag{9}$$

where η_{orig} is the reference value of the radial viscosity profile at the CMB, shown by the black line in Figure 1 and η_{red} is a reduced value of the radial viscosity profile at CMB, shown as colored lines in Figure 1. The radial viscosity profile between the CMB and 500 km above it is modified to ensure a smooth viscosity reduction toward the bottom, as demonstrated by colored lines in Figure 1. The radial viscosity profile above 500 km from the CMB is identical for all models. The range of viscosity reductions tested in this study is given by $0.25 < \gamma < 1.0$.

2.4. Numerical Solution

We have developed a finite element method (FEM) code with particle-in-cell methodology, building on efficient MATLAB routines from MILAMIN [*Dabrowski et al.*, 2008], together with packages MUTILS [*Krotkiewski*, 2013] and Triangle [*Shewchuk*, 1996].

The velocity is discretized with an unstructured triangular grid with high-order shape functions, using seven-node triangular elements. The pressure field within each element is discretized with a piecewise linear shape function. The global pressure field is thus discontinuous across element edges. For the numerical solution of the advection-diffusion equation (3), describing energy conservation, we employ the fractional step method, or Godunov splitting [*LeVeque*, 2002], for time discretization: pure advection is solved first, followed by the diffusion step. The diffusion equation is solved on an unstructured triangular grid with first-order (linear) shape functions. The thermal grid elements are generated by splitting each mechanical element into six triangles.

At regular time intervals throughout the simulation, we regenerate the static meshes, on which mass, momentum, and thermal diffusion equations are solved. The mesh is refined in regions of large thermal gradients. This refinement criteria improves the accuracy of the diffusion solver and also that of the mechanical solver. The latter is due to the exponential dependence of viscosity on temperature, due to which regions of large thermal gradients correspond to regions of strongly varying viscosity, which require higher resolution in order to sustain the desired level of accuracy [*Moresi et al.*, 1996; *Deubelbeiss and Kaus*, 2008; *Duretz et al.*, 2011]. Example

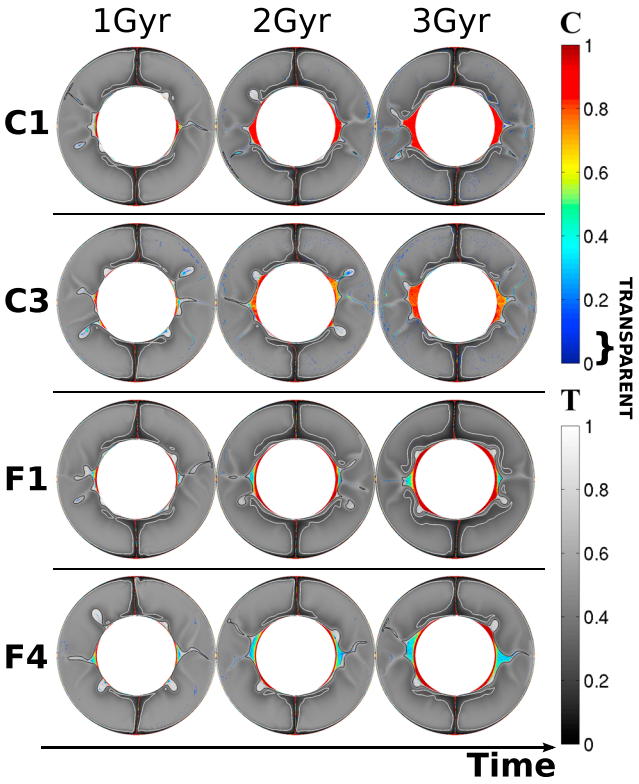

Figure 2. Snapshots of the thermochemical evolution at three points in time (1, 2, and 3 Gyr) for four different cases (from top to bottom): C1 (Br = 0.71, $\gamma = 1.0$), C3 (Br = 0.71, $\gamma = 0.50$), F1 (Br = 1.1, $\gamma = 1.0$), and F4 (Br = 1.1, $\gamma = 0.25$), as indicated on the left of the figure. The gray scale reflects the thermal field (bottom color bar), and the red-blue scale reflects the concentration of OC material (top color bar). Concentrations of OC material lower than 0.1 are made transparent.

of a grid which illustrates this spatial adaptivity scheme is shown in Figure S1 in the supporting information. The number of mechanical elements used for our simulations is $\approx 3 \cdot 10^5$, which corresponds to $\approx 1 \cdot 10^6$ grid nodes (number of nodes is equal for mechanical and thermal grids). When scaled to dimensional values, the characteristic spatial mesh resolution ranges from 30 km — in regions of lowest thermal gradients to 1 km — in regions of highest thermal gradients.

The advective component of equation (3), as well as equation (4), is solved using the characteristics-based marker-in-cell method [*Gerya and Yuen*, 2003; *Tackley and King*, 2003]. Markers, or tracers, are points in space in which the initial thermal and compositional field values are prescribed. During the advection step, positions of markers are updated, according to the computed velocity field, and using the second-order Runge Kutta method (mid-point rule) for computing the trajectories. The number of markers is generally larger (by at least an order of magnitude) than the number of grid nodes. We use $\approx 4.5 \cdot 10^7$ markers in our simulations, which on average results in $\approx 1 \cdot 10^2$ markers per mechanical element.

The code has been thoroughly tested for thermal and thermochemical convection, against benchmarks commonly used in the geodynamic community [e.g., *Van Keken et al.*, 1997; *Blankenbach et al.*, 1989]. Additionally, confidence in our numerical results was gained through convergence tests. In particular, four of the tested cases were simulated with $\approx 1 \cdot 10^5$ mechanical elements and $\approx 1 \cdot 10^7$ markers, i.e., ≈3 times fewer than what is used in our study. Time evolution of values of Nusselt number, root-mean-square velocity, and fraction of volume occupied by thermochemical piles obtained with the coarser resolution were found to be within the range of those obtained with higher resolution.

3. Results

We systematically vary two physical parameters that have been found to play a dominant role in the evolution of compositional anomaly in a vigorously convecting mantle: intrinsic density anomaly of the oceanic crust (OC) (prescribed through buoyancy ratio, equation (6)) and viscosity (prescribed through viscosity ratio γ in the bottom 500 km, see section 2.3). We use capital letters B–F to enumerate different *Br* values (B, C, D, E, and F correspond to *Br* = 0.57, 0.71, 0.85, 0.99, and 1.1, which scale to $\Delta\rho'_C$ = 100, 125, 150, 175, and 200 kg/m^3 or, equivalently, a density contrast of 1.8, 2.3, 2.7, 3.2, and 3.6%, respectively). Different γ values are indicated by numbers from 1 to 4 (1, 2, 3, and 4 correspond to $\gamma = 1.0$, 0.75, 0.50, and 0.25). For example, a model with *Br* = 0.57 and $\gamma = 0.50$ is entitled B3.

Figure 2 shows snapshots of the thermochemical evolution for four different cases: C1, C3, F1, and F4. In all of these cases, large-scale compositional anomaly is formed at the CMB. A zoomed-in view on piles that have developed by the end of each simulation (at 3 Gyr) is shown in both Figures 3 and 4 for the piles on the left

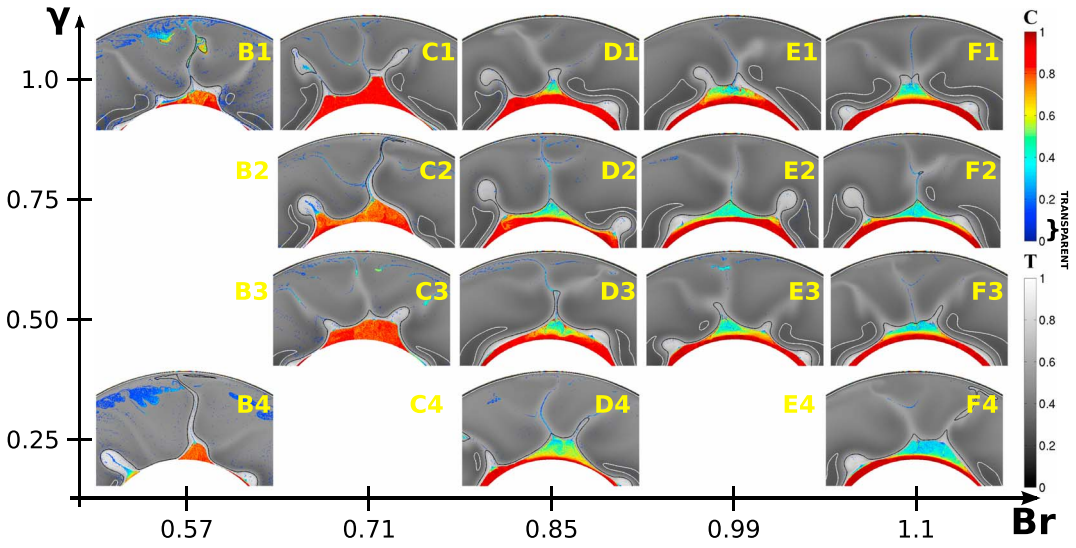

Figure 3. Snapshots at 3 Gyr for all studied cases, zoomed-in on the thermochemical pile that develops on the left side of the domain. The gray scale reflects the thermal field (bottom color bar), and the red-blue scale reflects the concentration of OC material (top color bar). Concentrations of OC material lower than 0.1 are made transparent.

and right sides of the domain, respectively. The shapes of large-scale anomalies in the presented cases can be grouped into two categories:

1. Large topography piles with sharp edges, which are highly mobile both laterally and vertically, have a close to homogeneous distribution of dense material in their interior and have plumes rising from their surface and edges, occasionally entraining large bulks of the pile material;
2. High-density basal layer covering nearly the entire CMB, overlain by high-topography piles with a much lower fraction of OC material, and plumes rising from their interior and edges, entraining thin filaments of pile material.

Scenario (1) is typical for the cases with moderate buoyancy ratio (Br < 0.8), while scenario (2) is typical for the high buoyancy ratios (Br > 0.8). The effect of lowering viscosity in the bottom 500 km appears to reduce the concentration of dense material in the piles.

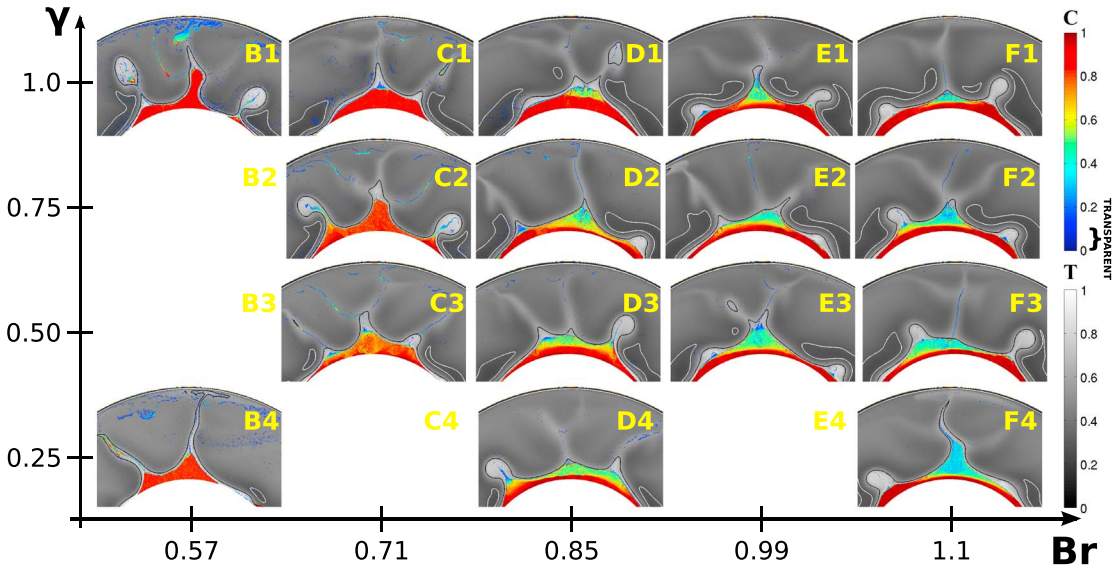

Figure 4. Same as Figure 3, but zoomed-in on the thermochemical pile that develops on the right side of the domain.

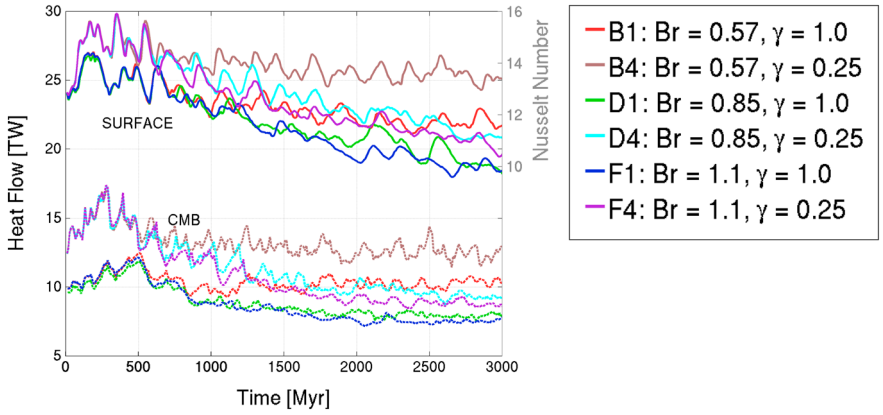

Figure 5. Time evolution of conductive radial heat flow across the surface (solid lines) and the CMB (dashed lines). Dimensional values (in TW) are indicated on the left axis and were obtained by first dimensionalizing the values of circumference-averaged conductive radial heat flux, measured at the top and bottom boundaries of the models and then integrating these values over the spherical surface area of the Earth and CMB, respectively. Note that this results in exaggerated difference between net surface and net CMB heat flux in this plot, due to a smaller ratio of top to bottom "surface areas" in 2-D, compared to those in 3-D. Right axis indicates the respective values of the Nusselt number (only shown for the surface heat flux).

3.1. Global Scale Time Evolution

Figure 5 shows time evolution of heat flow, measured at upper and lower boundaries of the model, for six different cases (B1, B4, D1, D4, F1, and F4). The right axis of Figure 5 shows the respective values of the Nusselt number (*Nu*)—the nondimensional radial conductive heat flux at the surface of the cylindrical (2-D) model. Results of Figure 5 demonstrate the effect of buoyancy ratio and viscosity reduction in the bottom 500 km on our models' thermal evolution. *Nu* in the beginning of the simulations (up to 1 Gyr–before any substantial amount of dense material has been accumulated at the bottom) is very similar for cases with the same values of viscosity: lowering the viscosity in the bottom 500 km leads to higher heat flux at the surface, consistent with the fact that a lower viscosity gives a higher effective Rayleigh number—thus, a higher vigor of convection and more efficient heat flux. After approximately 1 Gyr, the effect of the accumulated dense material at the base becomes evident: cases with the higher buoyancy ratio and, thus, a larger volume of dense material accumulating on top of the CMB (as will be discussed in Figure 6), have a lower *Nu*, compared to cases with lower *Br*. Highest *Nu* (from ~1.5 Gyr until the end of the simulation) among the presented models is obtained for the case with the lowest buoyancy ratio and lowered viscosity in the bottom 500 km (B4: $Br = 0.57$, $\gamma = 0.25$), and the lowest *Nu* is obtained for the case with the highest buoyancy ratio and original (i.e., not reduced in the bottom 500 km) viscosity profile (F1: $Br = 1.1$, $\gamma = 1$).

Presence of a large-scale compositionally dense anomaly at the bottom of the mantle reduces the heat flow across the CMB. This is shown for six different cases in Figure 6a, where the amount of dense material that accumulates at the base of the mantle is plotted against the decrease in mean temperature at mid-depth from its initial value. The result shows that a larger amount of high-density material at the CMB leads to a cooler system. A cooler midmantle is also more viscous, due to the temperature dependence of viscosity. Thus, the mantle, in cases with more dense material at the base, is more viscous and has a lower effective Rayleigh number. Figure 6a also shows that more dense material accumulates at the base for higher values of *Br*, meaning that increasing *Br* leads to a cooler and more viscous mantle. The effect of decreasing viscosity in the bottom 500 km on the amount of dense material that gets accumulated at the base is less pronounced. It appears that for cases with $Br < 0.8$, decreasing γ reduces the amount of material that gets accumulated, while for cases with $Br > 0.8$, decreasing γ slightly enhances accumulation.

Figure 6b shows the volume fraction of the dense OC material present in the system for the six cases over time. The downwelling flow in our models, and thus exposure of new surface area where OC can form, is largely determined by the prescribed surface velocities and is therefore similar for all of the models. According to the current rate of production of OC, as well as that of the recent past, *Xie and Tackley* [2004] estimate that the OC constitutes approximately 10% of the mantle volume today. This is a double value of what is produced in our models by the end of the simulations, meaning that our modeled rate of replenishment of the high-density OC material is lower compared to a more Earth-like system.

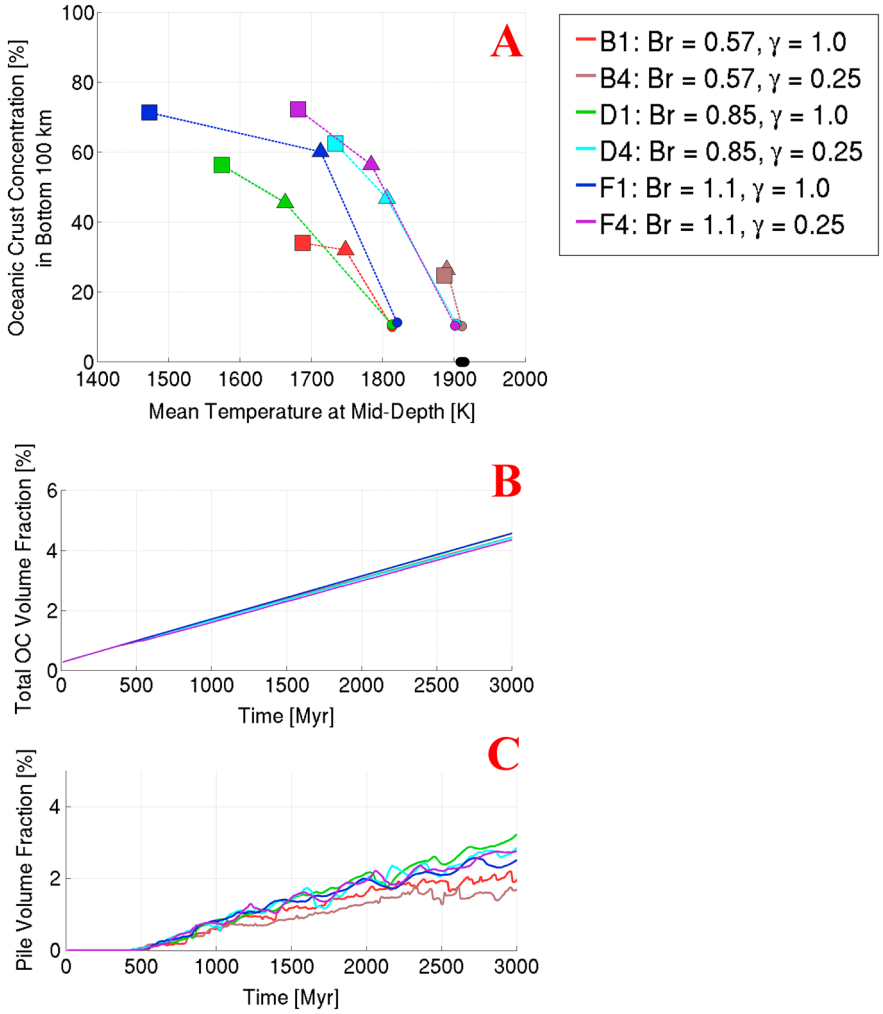

Figure 6. (a) Mean temperature at mid-depth versus mean concentration of OC material in the bottom 100 km of the domain. Results for six cases are presented according to legend. Colored symbols indicate points in time at which the plotted values were sampled: circles-0.5 Gyr, triangles-2 Gyr, and squares-3 Gyr. The black filled circles are the values sampled after the first 10 Myr of the simulation. (b) Volume fraction of OC material present in the system over time. (c) Volume fraction occupied by thermochemical piles over time.

Figure 6c shows how the size of thermochemical piles at the CMB changes through time. We observe that by the end of the simulations, the volume fraction occupied by the piles is comparable with the values estimated for the seismically observed LLSVPs—~2%. Growth rate of the piles in cases with lower *Br* values (B1, B4) appears to be declining with time, while in the cases with high *Br* values (D1, D4, F1 and F4), the growth rate appears to remain more or less constant.

Upwelling flow of the rising hot plumes can entrain the high-density OC material in its vicinity and gradually contribute to the destruction/erosion of the accumulated dense anomaly at the CMB. This can happen solely by the action of viscous drag, in which case only a thin filament of high-density material is entrained. This is observed in cases with $Br > 0.8$ (Figures 3 and 4). Entrainment can be assisted by the action of mechanical mixing of high-density and ambient materials prior to rising in plumes: a sufficiently diluted mixture can be heated to the degree where its effective compositionally induced positive density anomaly is less strong than the thermally induced negative density anomaly, forming the so-called thermochemical plumes. The latter is observed in cases with $Br < 0.8$ (Figures 3 and 4) and is much more efficient at destroying the compositional anomaly at the base of the mantle—i.e., it causes a higher flux of high-density material from the bottom to the surface of the mantle. Efficiency of these two entrainment modes to transport high-density material is demonstrated in Figure 7, where volume flux of OC material across mid-depth is plotted over time for six different cases (negative flux means in the direction upward from the CMB). The plotted volume flux of OC

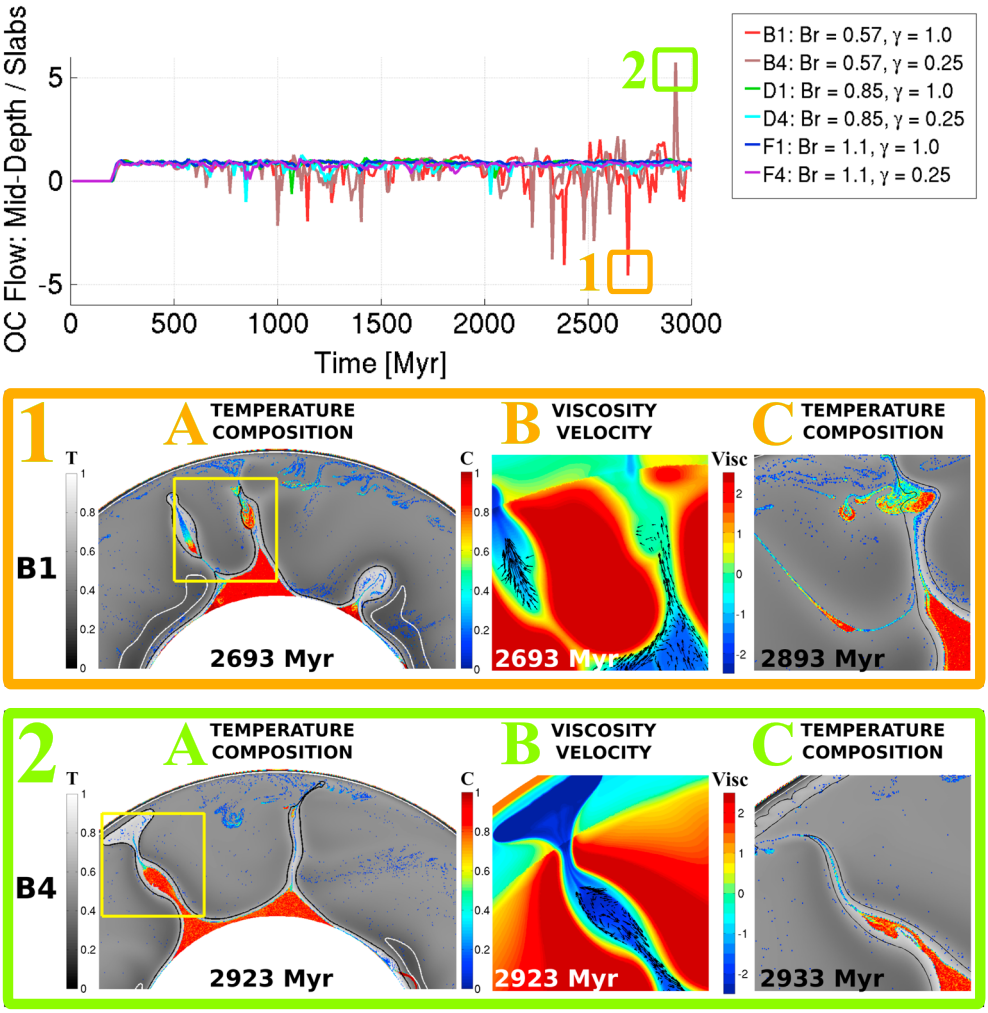

Figure 7. (top) Volume flux of OC material measured at mid-depth of the domain for six cases (see legend), scaled by the volume flux of OC material transported by subducting slabs. Negative flux means in the direction upward from CMB. Events associated with one of the negative peaks (orange box) in case B1, and one of the positive peaks (green box) in case B4 are explained in the inserts 1(A–C) and 2(A–C), respectively. (1A and 2A) Temperature and composition fields for one of the piles at the time of their respective peaks, with yellow square marking the region of zoom in in 1(B and C) and 2(B and C), respectively. (1B and 2B) Velocity and decadic logarithm of viscosity fields at the time of the peak. (1C and 2C) Temperature and composition fields some time after the observed peak in OC flow.

is normalized by that associated with the two downwelling regions, which is governed by prescribed surface velocities and is similar for all cases. The rise of well-stirred thermochemical plumes, reflected in the large negative peaks of OC flux in Figure 7, is observed for cases with $Br < 0.8$. An example of one such event for case B1 is shown in the insert in Figure 7. In some cases, thermochemical plume fails to rise all the way to the surface, and a part of it drains back down. In one such example, shown for case B4 in the second insert of Figure 7, the hottest, least viscous, and closest to center (i.e., farthest from surrounding ambient mantle) part of the plume drains down, while the rest of the plume continues to rise. Such rare events are reflected in the positive peaks of OC flux in Figure 7. For cases with $Br > 0.8$, entrainment of dense material by plumes is very inefficient—the net OC flux across the midmantle exhibits very rare (if any) and small in amplitude negative peaks.

To visualize the individual events associated with variations in entrainment and heat flux, we present the volumetric flux of OC material and heat flux as functions of time and azimuthal position in Figure 8, measured at mid-depth of the domain for five different cases (B1, B4, C3, F1, and F4). Figure 8 illustrates the episodic nature of plumes—the yellow-red dots in the heat flux part of the figure. It is interesting to see the locations of plumes with respect to the locations of the thermochemical piles. For this purpose, we superpose the locations

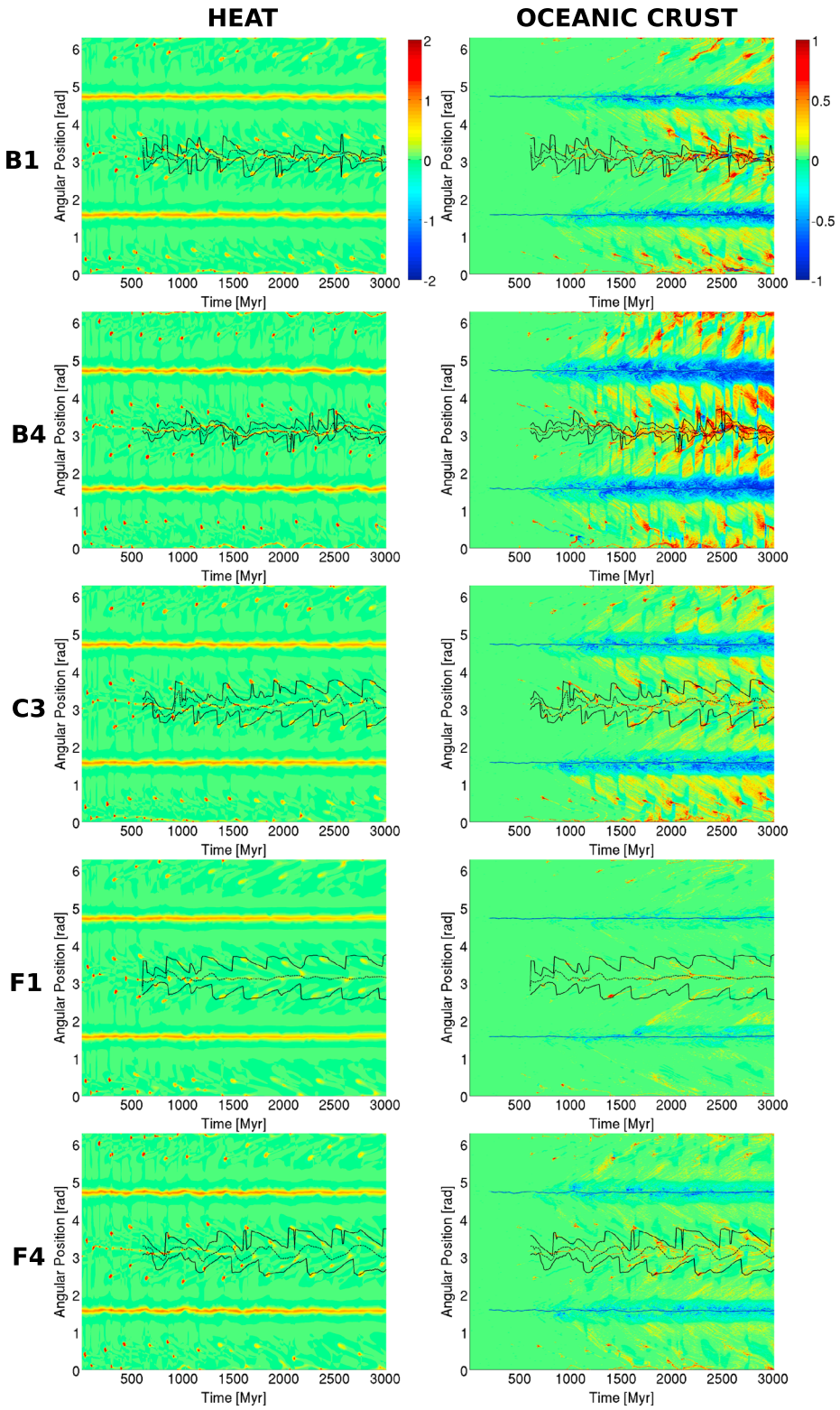

Figure 8. Dimensionless (left) heat flux and (right) volume flux of OC material, both measured at mid-depth of the domain, as functions of time and azimuthal position for cases B1, B4, C3, F1, and F4. Heat flux color bar $[-2, 2]$ translates to dimensional values of $\sim[-25, 25]$ kW/m. Flux of OC material is positive when it is away from the CMB, and its color bar $[-1, 1]$ translates to dimensional values of $\sim[-18, 18]$ m^2/yr. The black solid lines superposed on top of each figure indicate the "north" and "south" boundaries for one of the piles. Pile boundaries are evaluated for the part of the pile that is above its average height over CMB. The dashed black line indicates the mean lateral position of the pile.

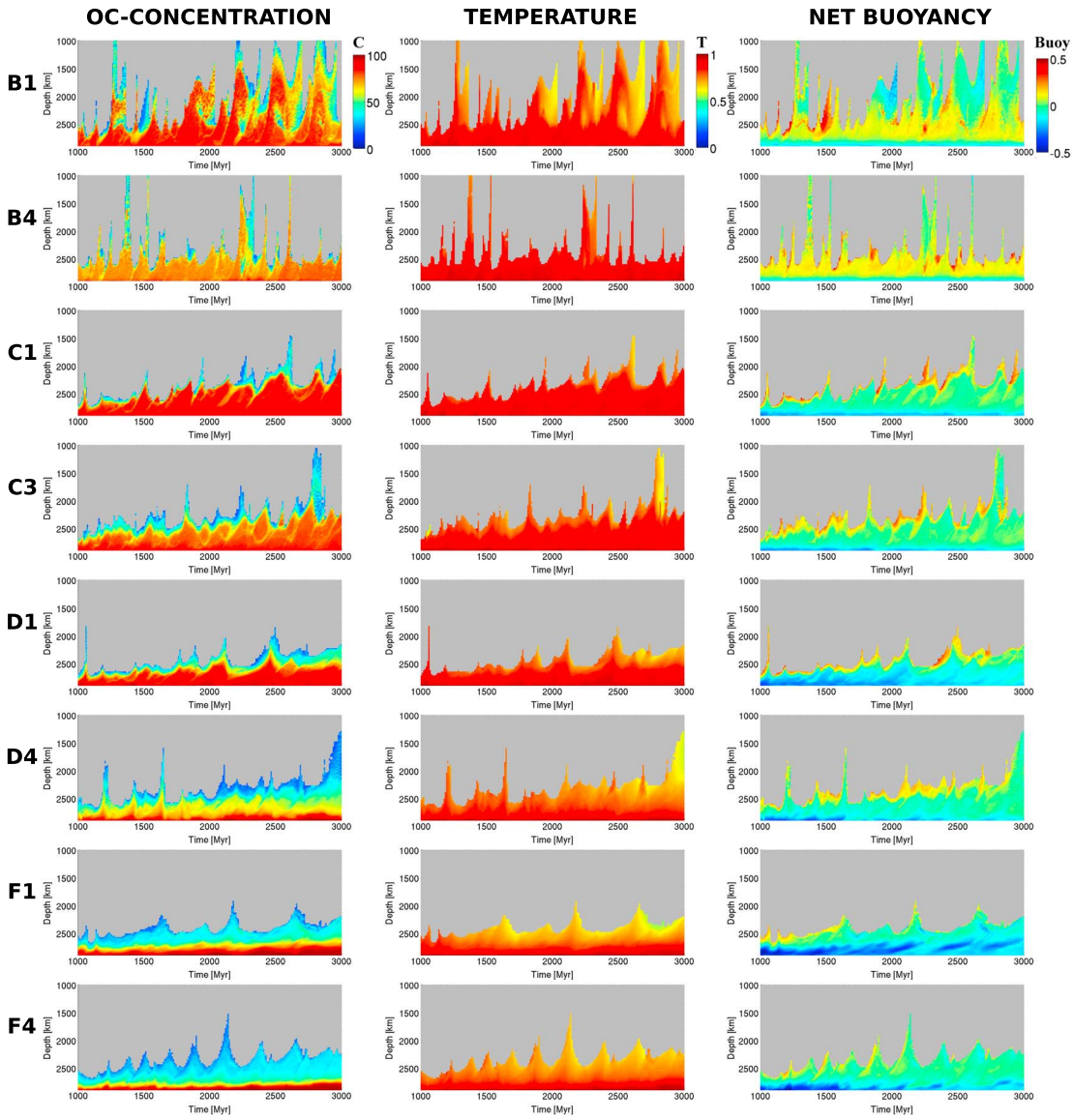

Figure 9. Time evolution of concentration of the (left) OC material, (middle) temperature, and (right) total buoyancy anomaly in the thermochemical piles, as functions of time and depth. Results for the piles on the left side of the domain for eight different cases are shown, as indicated on the left of each row: B1, B4, C1, C3, D1, D4, F1, and F4. See Text S2 in the supporting information for technical details on how we distinguish thermochemical piles from the rest of the mantle.

(black lines) of the "north" and "south" boundaries for one of the piles in each simulation onto the heat flux and OC flux color plots in Figure 8.

We can identify three typical locations of plumes with respect to the piles: close to both edges of the pile and the mean lateral position of the pile. The plumes occurring close to the mean lateral position of the pile are cooler and more long-lived, compared to the ones occurring at the edges. Cases with lower viscosities in the bottom 500 km of the domain (B4 and F4) exhibit higher plume frequency and hotter plumes, compared to their more viscous counterparts (B1 and F1). Plumes are colder and less frequent in cases with high buoyancy ratio (F1 and F4), where a high-density layer develops on top of the CMB.

The contours of the piles in Figure 8 illustrate the transient, or oscillating, nature of the piles geometry: it shrinks and expands laterally over time and also moves as a whole laterally along the CMB.

Transport of OC material across mid-depth in cases with high *Br* (F1 and F4) is mostly restricted to the narrow regions associated with the downwellings—downward transport of the OC, as well as the highly localized regions where the OC material is transported upward. The latter is associated with the thin filaments of

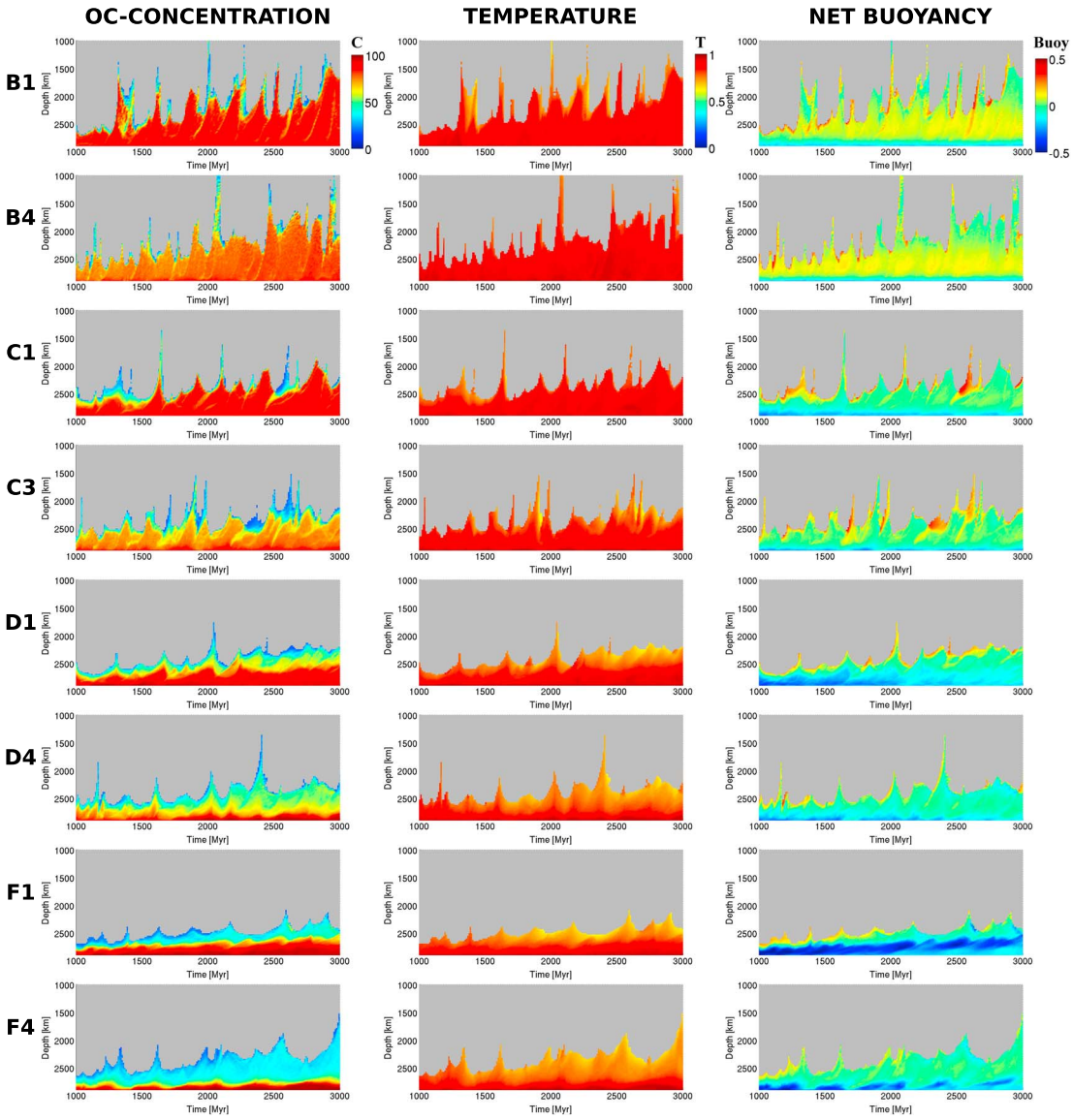

Figure 10. Same as Figure 9 but for the thermochemical piles on the right side of the domain.

high-density material entrained by plumes. In contrast, in cases with a moderate buoyancy ratio (B1, B4, and C3), a lot more OC material is traversing the mid-depth of the domain—illuminating both the fact that plumes carry more of the dense material as they rise and that there is a larger fraction of dense material present as a well-stirred component of the ambient material. In all cases, a Christmas-tree-like structure can be seen in the plots of the OC material flux, which indicates that plumes carrying high-density material upward tend to migrate toward the center of the piles.

3.2. Pile Scale Time Evolution

For a more detailed analysis of the internal structure of thermochemical piles, we look at the time dependence and depth dependence of the following parameters measured in their interior: concentration of the OC material, temperature, and the total buoyancy anomaly. The latter is defined as the sum of thermally and compositionally induced density variations inside the pile, with respect to the azimuthally averaged values of temperature and composition in the ambient mantle. Results are presented in Figures 9 and 10.

OC Concentration. All piles presented in Figures 9 and 10 exhibit some degree of vertical stratification of OC concentration, which generally decreases away from the CMB. Intermittently appearing regions

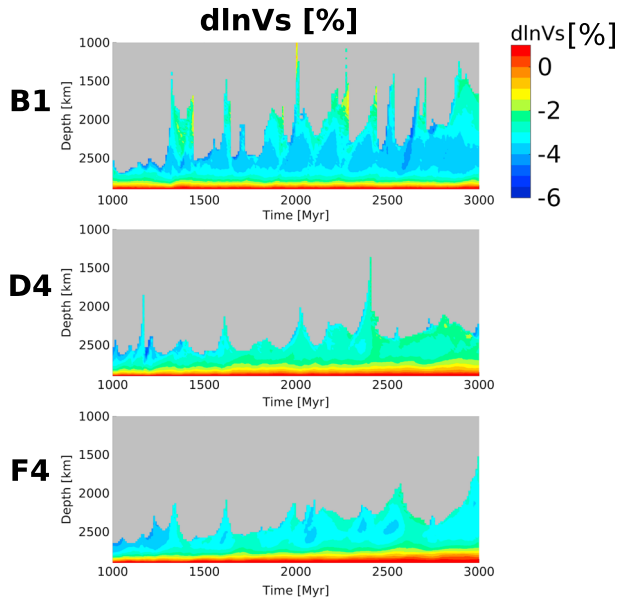

Figure 11. Evolution of azimuthally averaged shear wave velocity anomaly ([%] $\mathrm{dln}V_S$) in the interior of thermochemical piles, as functions of time and depth, for three selected cases: B1, D4, and F4. Results for piles developing on the right side of the domain are shown. Sensitivity values used for the dependence of shear wave velocity anomaly on temperature anomaly and concentration of OC material are within the uncertainty range of values suggested by *Trampert et al.* [2004] and *Deschamps et al.* [2012]: $\mathrm{dln}V_S/\mathrm{d}T = -3.1 \cdot 10^{-5}$ K^{-1}, and $\mathrm{dln}V_S/\mathrm{d}X_{\mathrm{MORB}} = 0.3 \cdot 10^{-1}$, where X_{MORB} stands for a fraction of MORB or OC material.

of extremely low OC concentrations (< 20%) at the surface of the piles, which get rapidly removed upward, indicate entrainment by plumes.

In cases with $Br < 0.8$, OC concentrations in piles interior is more homogeneous (compared to those with $Br > 0.8$), at a value between ~80–90% for cases with $\gamma = 1$ (B1 and C1), and between ~65–75% for cases with $\gamma = 0.25$% (B4 and C3). Piles in cases with $Br > 0.8$ exhibit more vertical stratification of OC concentration in their interior. Two regions can be distinguished in these cases (least pronounced for case D4 in Figure 9): a high concentration (~90–100%) region at the bottom, overlain by a low-concentration (~40–60%) region. In cases with $\gamma = 1$ (D1 and F1), the high-concentration regions are thicker and the low-concentration regions are thinner, compared to their counterpart cases with $\gamma = 0.25$ (D4 and F4).

Temperature. Temperature distribution in the piles interior can also be grouped between cases with $Br < 0.8$ and those with $Br > 0.8$: cases with $Br < 0.8$ exhibit close to a homogeneous thermal structure (T ~0.8–0.9, or T' ~2850–3150 K), while cases with $Br > 0.8$ have a notable thermal gradient, with cooler pile surfaces (T ~0.6–0.7 or T' ~2200–2500 K).

Net Buoyancy Anomaly. The net buoyancy of the piles with respect to the ambient mantle, shown in Figures 9 and 10, illustrates that neutrally buoyant thermochemical structures developed in all of the presented cases and are persistent features that, once developed, survive for several billion years. For cases with $Br > 0.57$ the net buoyancy of the piles generally falls in the range between neutral and negative, with a negatively buoyant bottommost part and buoyancy increasing upward until it reaches the level of neutral buoyancy. In contrast, piles developing in cases with $Br = 0.57$ (B1 and B4) are positively buoyant (albeit only slightly) in the largest fraction of their interior, except for the negatively buoyant bottommost part and a neutrally buoyant uppermost part. Such buoyancy structure develops due to the variation of azimuthally averaged temperature with depth. Starting from the CMB, the value of azimuthally averaged temperature decreases upward, until it reaches the depth of ~2600 km, at which point it starts rising again until it reaches its adiabatic value at ~1500 km depth. Thus, as the positively buoyant thermochemical pile rises through the mantle in the depth range ~2600–1500 km, it is surrounded by an increasingly hotter mantle, which lowers the effective buoyancy of the pile until neutral buoyancy is reached. A positively buoyant lower part of a pile that underlies its neutrally buoyant part was also observed in *Tan and Gurnis* [2005], who suggested such buoyancy structure to be a plausible explanation for high topography yet gravitationally stable thermochemical piles at the bottom of the mantle. The mechanism that generated such buoyancy structure in their case, however, was depth dependence of the compositionally induced density anomaly due to the different equations of state used for the ambient and dense materials.

The seismic signal associated with OC material in the lower mantle is currently debated [*Tsuchiya*, 2011; *Deschamps et al.*, 2012]. However, just to give an estimate of what the seismic shear wave velocity anomaly may look like for the piles developing in our simulations, we present a plot of its azimuthally averaged value for three selected cases in Figure 11. We use sensitivity values for the dependence of shear wave velocity anomaly on temperature anomaly and concentration of OC material that are within the uncertainty range

of values suggested by *Trampert et al.* [2004] and *Deschamps et al.* [2012]: $d\ln V_S/dT = -3.1 \cdot 10^{-5} K^{-1}$, and $d\ln V_S/dX_{MORB} = 0.3 \cdot 10^{-1}$, where X_{MORB} stands for a fraction of MORB, or OC material. With this choice of values, large portions of piles interior have a shear wave velocity reduction between $\sim -4\%$ and -2%, in agreement with seismic observation (see section 4.4 for details). In their bottommost part, however, contrary to what is seismically observed, the anomaly becomes positive. This is likely due to a number of reasons, including: (i) vanishing lateral thermal anomaly within the thermal boundary layer, (ii) constant value of $d\ln V_S$, as opposed to one that gets more negative toward CMB in the lowermost mantle (as in *Steinberger and Calderwood* [2006]), and high concentration of OC material at the bottom of the piles, which has a positive shear wave velocity anomaly associated with it. We emphasize that the sensitivity values used to generate these results are subject to debate.

4. Discussion

4.1. Main Findings From Numerical Simulations

For a range of parameters tested in this study — intrinsic density of the oceanic crust (OC) (Br, equation (6)) and viscosity in the bottommost 500 km of the mantle (γ, equation (9)), a large-scale compositional anomaly forms at the CMB from the segregated OC. Once formed, the large-scale anomaly survives for several billion years. Formation and long-term survival of the thermochemical piles occur in our models despite the low influx rate of OC material, which results from a low value of the tectonic plates velocity prescribed at the surface. Low influx of OC material together with excessively strong upwelling flow (due to absence of internal heating) constitute unfavorable conditions for the formation of the piles. On the other hand, the prescribed stable locations of the downwelling regions, where the dense OC material gets transported into the mantle depth, facilitates the formation and survival of thermochemical piles. Strong thermally induced viscosity variations present in our models also favor segregation of OC material to the CMB and subsequent formation of thermochemical piles with highly heterogeneous internal structure. In agreement with previously published, both numerical and experimental studies, increasing buoyancy ratio promotes segregation, accumulation, and survival of the dense material at the CMB [*Olson and Kincaid*, 1991; *Christensen and Hofmann*, 1994; *Nakagawa and Tackley*, 2005; *Brandenburg and Van Keken*, 2007; *Huang and Davies*, 2007].

4.2. Density Anomaly of Thermochemical Piles

In cases with moderate values of $Br = 0.57$ and 0.71, the neutrally buoyant piles contain ~80% of dense OC material, which scales to a net compositionally induced density anomaly associated with the piles of ~80 and 100 kg/m^3, respectively, or, equivalently, of 1.45% and 1.82%. This is consistent with the preferred compositional density anomaly value of $\sim$ 2% in previously published experimental and numerical results of thermochemical mantle convection, which uses a dense basal layer as part of their initial conditions, which subsequently evolves into LLSVP-like thermochemical piles [e.g., *Davaille*, 1999; *Davaille et al.*, 2002; *Kellogg et al.*, 1999; *Tackley*, 2002; *Zhong and Hager*, 2003; *Tackley*, 2012]. For high values of $Br = 0.85$, 0.99, and 1.1, a dense layer (concentration of OC ~100%) forms at the base of the mantle, and a neutrally buoyant pile develops on top of it (concentration of OC ~30%). This scales to a compositionally induced density anomaly associated with the dense layer of ~150, 175, and 200 kg/m^3 (equivalent to 2.72, 3.18, and 3.64%), respectively and that associated with the overlying neutrally buoyant piles of ~45, 52, and 60 kg/m^3 (equivalent to 0.82, 0.95, and 1.09%), respectively. The dense basal layer and the neutrally buoyant pile on top of it are clearly separated by a jump in the concentration of the compositionally anomalous material (Figures 9 and 10). These values for the compositional density anomaly of thermochemical piles are difficult to compare to previously published models, because, to our knowledge, such vertically stratified structures have not been observed before.

In cases with both moderate and high *Br* values, the shapes of the neutrally buoyant piles vary through time between ridge-like and dome-like.

The observed spatial distribution of the OC material within the large-scale anomalies can be grouped into two categories:

1. large topography piles with sharp edges, which are highly mobile both laterally and vertically, have a homogeneous distribution of dense material in their interior, and have plumes rising from their surface and edges, occasionally entraining large bulks of the pile material;

2. high-density basal layer covering nearly the entire CMB, overlain by high-topography piles with a much lower fraction of OC material, and plumes rising from their interior and edges, entraining thin filaments of pile material.

Scenario (1) is typical for the cases with moderate buoyancy ratio (Br < 0.8), while scenario (2) is typical for high buoyancy ratios (Br > 0.8). The role of reduced viscosity in the bottom 500 km is to decrease the concentration of the OC material in the pile, resulting in a more diluted — and thus more positively buoyant — mixture (Figures 3, 4 and 9, 10).

Concentration and spatial distribution of dense material within the piles is strongly influenced by the motion in the piles interior. It can be induced by small-scale convective heat transport, due to heat flowing from the CMB, given that the piles *Ra* number is above critical (e.g., that the pile is sufficiently thick). Motion within the pile can also result from plumes rising in its vicinity — due to viscous coupling of the two. Lowering viscosity in the lowermost mantle is expected to increase the internal motion of the pile — both due to the resulting increase in the piles local *Ra* number and due to higher velocity of the material rising in plumes in the vicinity of the piles. The effect of the latter can be somewhat compensated by the decrease in viscous drag, as drag itself is also proportional to viscosity.

Motion within the pile also affects the spatial distribution of dense and ambient materials in its interior, with more vigorous motion resulting in more homogeneous distribution. Distribution of the pile materials toward a homogenized well-stirred mixture is opposed by the effect of buoyancy, which arises due to the intrinsic density difference between the materials. Buoyancy acts to create a higher concentration of dense material closer to the CMB and a lower concentration closer to the surface of the pile. Increasing the buoyancy ratio is thus expected to result in more (vertically) heterogeneous compositional structure. This is, indeed, what is observed in Figures 3, 4: for a given viscosity structure, increasing the density anomaly of the OC material leads to a more vertically stratified distribution of dense material in the pile.

4.3. Processes Responsible for Heterogeneous Internal Structure of Thermochemical Piles

To gain some physical intuition into the processes responsible for the observed behavior and evolution of thermochemical piles, it is helpful to think of the piles and the rest of the mantle as two separate systems. A pile represents a reservoir linked to the rest of the mantle through exchange of heat and material. Heat enters the pile by diffusion from the hot CMB. Heat escapes the pile through diffusion across the interface between the pile and the ambient material, as well as through (i) influx of the newly arrived cold dense material, (ii) influx of the cold ambient material by entrainment (due to the motion within the pile), and (iii) departure of the hot pile material that gets entrained into hot rising plumes. Processes (i)–(iii) also describe the material exchange between the pile and the ambient mantle.

It is reasonable to assume that the rate at which dense OC material enters the pile (process (i)) is more or less constant throughout the simulation time. This is because this process is governed by the rate of subduction, which brings the dense material to the CMB, and which is controlled by the prescribed surface velocities. The rate at which ambient material enters the pile (process (ii)) is determined by the interior motion of the pile and viscosity in the vicinity of the interface between the pile and the ambient material.

Formation of a dense basal layer takes place when process (i) — influx of the newly arrived dense material – dominates over processes (ii) and (iii) — influx of ambient mantle material into pile (or layer), and entrainment of pile material into plumes. As the basal layer continues to grow - the temperature at its surface sinks, as it rises further away from the CMB. Lower temperature leads to higher viscosity at the surface of the layer — and thus stronger drag imposed on the layer by the thermal plumes rising off its surface. Increasingly strong viscous drag destabilizes the dense material at the surface of the layer. Plumes may not always manage to carry a thin filament of dense material all the way up to the surface, and the initially entrained filament collapses back onto the surface of the layer. The filament does not collapse alone, however, but with a fraction of ambient mantle material viscously coupled to it. Repeated action of this process of entrainment and collapse is responsible for the formation of a secondary thermochemical pile on top of the dense basal layer. Due to the elevated viscosity within this low OC concentration secondary pile (compared to the low-viscosity and high temperature layer closer to the CMB), as well as the small thickness of the destabilized filaments (due to high buoyancy ratio — viscous drag is only capable of destabilizing very small volumes of dense material), the dense material within the secondary pile is prevented from segregating back to rejoin the dense basal layer. The observed stability of the neutrally buoyant low OC concentration pile on top of the dense basal

layer points to the balance in the rate at which new dense filaments are formed and start contributing to the pile, and the rate at which plumes manage to carry the pile material away—all the way up to the surface.

Our modeling results suggest that the domains in the diagram from *Le Bars and Davaille* [2004, Figure 2], which classifies different patterns observed in thermochemical convection at different buoyancy and viscosity ratios (albeit in their case—both due to intrinsic material properties), are not model-specific. Rather, several domains can be present within one system: a thin dense basal layer where conduction is the dominant heat-transport mechanism, underlying a flat layer that is internally convecting, which is overlain by a high-topography layer with yet lower concentration of dense material, and—the cherry on top—the neutrally buoyant oscillating dome topping off the large-scale compositional anomaly. Compositionally dense material that fails to become a part of the aforementioned structures gets stirred and thinned by ambient flow and eventually becomes dynamically indistinguishable from the ambient mantle. If the intrinsic density of compositionally anomalous material (OC in our case) is too low to form any of the dense basal layers—only the neutrally buoyant high-topography pile is observed. For yet lower values of intrinsic density—no material manages to segregate, and the two materials mix and eventually form a homogeneous mixture.

4.4. Comparison With the Seismologically Observed Structure of LLSVPs

In our simulations, neutrally buoyant thermochemical piles—those in which the thermally induced negative density anomaly is balanced by the presence of high-density OC material—best resemble the geometry of LLSVPs: high topography of over 1000 km with steep edges (Figures 3, 4) and occupying a few percent (~2%) of the total 2-D volume (Figure 6c). Interestingly, such neutrally buoyant piles tend to emerge and survive for a long time (several gigayears) in simulations that span a large range of tested values for parameters such as density and viscosity (yet within the proposed range of uncertainty of these parameters). Both internal and exterior structure of piles that develop in models with different values of Br and γ exhibit great degree of variation, including variation through time for each individual model. It is interesting to compare these geometrical characteristics with those of LLSVPs, which are derived from seismic observations.

The African LLSVP appears to have a ridge-like [*Ni and Helmberger*, 2003] structure with dimensions of about 1000 km ×7000 km laterally [*Ni and Helmberger*, 2003] and extending up to 1300–1500 km above the CMB [*Ni and Helmberger*, 2003; *Wang and Wen*, 2007]. *Wang and Wen* [2007] describe the geometry of African LLSVP in terms of two portions (without any separating gap): part (i) is in the mid-mantle, has a bell-like shape, and its associated average shear velocity reduction is of −2% to −3%; part (i) is underlain by part (ii), which is a 150 to 250 km thick layer with an associated average shear velocity reduction of −5%. Observations of *Ni and Helmberger* [2003] and *Wang and Wen* [2007] agree that the lateral extent of African LLSVP increases with depth. Similar pile geometries can be observed in our numerical results, in particular, cases D4 and F4 in Figure 3, and cases D2, E2–E3, and F2–F4 in Figure 4. We note, however, that the geometry of piles developing in each of our models change through time, and a different set of cases may be consistent with these observations at a different point in time.

Pacific LLSVP appears to have a more rounded structure [*He and Wen*, 2009]. *He and Wen* [2009] identify two unconnected portions (with a 740 km wide gap in between) that constitute this anomaly: part (i) extends 1050 km laterally and 740 km above the CMB, has a shear wave velocity reduction of −3% to −3.5% (from its top to 100 km above CMB) and −5% (in the bottom 100 km) associated with it, and a trapezoid-like shape (widening with depth); part (ii) extends 1800 km laterally and 340 km above the CMB, and has a uniform shear wave velocity reduction of −3% associated with it. We do not observe such clearly separated portions of the large-scale anomalies in our models, although piles in cases C1–C2 in Figure 3 and those in cases B1 and C2 in Figure 4 can be seen as a taller pile portion connected by a thinned "bridge" to a portion with lower topography. In addition, case C2 in Figure 3 and cases C2–C3 in Figure 4 exhibit intermittent regions of higher OC concentrations (and also higher temperature) in the bottommost 100 km (also seen for case C3 in Figure 10).

Shear wave velocity reduction of −2% to −3.5% observed for the LLSVPs interior are broadly consistent with our results (Figure 11), although the sensitivity values that are needed to compute the synthetic seismic signal are currently uncertain [e.g., *Deschamps et al.*, 2012]. On the contrary, the observed shear wave velocity reduction down to −5% in the bottommost part of LLSVPs is the exact opposite of what we observe in our models, in which the anomaly reaches positive values close to the CMB.

5. Conclusions and Outlook

The following conclusions can be derived from the results of our thermochemical mantle convection simulations:

1. For a plausible range of values of density anomaly of OC material in the lower mantle — 100 – 200 kg/m^3 — it is likely that it segregates and accumulates at the CMB.
2. Once segregated, the dense material undergoes mechanical stirring that acts to create a large-scale compositional anomaly with a heterogeneous internal structure — both in terms of concentration of dense material and temperature.
3. Neutrally buoyant thermochemical piles develop in all of our studied cases, through mechanical mixing of OC material with the ambient mantle. These large-scale compositional anomalies are similar in shape to the seismically observed LLSVPs. Magnitude of the compositionally induced density anomaly associated with the neutrally buoyant parts of these structures ranges from 45 to 100 kg/m^3, depending on the intrinsic density anomaly of OC material in the lower mantle and distribution of OC material within the piles.
4. In cases with moderate buoyancy ratios, the neutrally buoyant piles develop directly on top of the CMB. Their interior does not exhibit any significant radial trends in OC concentration or temperature, but there exist, however, transient thermal and compositional heterogeneities.
5. In cases with moderate buoyancy ratios, neutrally buoyant thermochemical plumes are observed, which are efficient at transporting high-density material upward from the CMB, and thus at destroying the compositional anomaly. Such events are relatively rare and require a preliminary action of mechanical stirring at the bottom of the mantle — to form a diluted mixture of ambient and dense materials that constitutes the thermochemical plume.
6. In cases with high buoyancy ratios, the neutrally buoyant piles develop on top of a high-density (i.e., high OC concentration) layer, which forms prior to pile formation, and covers a large fraction of the CMB.
7. In cases with high buoyancy ratios, rising plumes are significantly colder than the ones developing in moderate buoyancy ratio cases and only manage to entrain thin filaments of high-density material as they rise.
8. Based on the comparisons between our numerical models and previously published seismological observations, we propose that the observed internal and exterior structure of LLSVPs reflects their internal distribution of high-density material. The latter is governed by motion in LLSVPs interior, which is in turn governed by values of intrinsic density anomaly and of viscosity in the lowermost mantle.

As a possible outlook, these results, in addition to illuminating some of the complexity of deep Earth dynamics, can predict possible structures that may develop in the interior of the large-scale heterogeneities, such as the LLSVPs. These predictions can then be tested against the results of seismological studies and thus serve as an additional constraint on models of the deep mantle. Further building on these results, it would be interesting to look at the effect that various possible structures of LLSVPs have on the thermochemical plumes that rise in their vicinity: e.g., thermal anomaly associated with the plumes, amount of OC material that they bring up to the surface, and evolution of these plume-characteristics through time. Such quantities predicted from numerical models can be tested against surface-observations of basaltic volcanism that are thought to be manifestations of deep mantle plumes.

Appendix A: Model Limitations

A1. Boussinesq Approximation

Assuming incompressibility of the mantle across its depth is not a fully justified approximation for mantle-like thickness and material properties [e.g., *Schubert et al.*, 2001]. While some purely thermal mantle convection studies have shown that compressibility may not play a crucial role in determining its convective pattern [*Bercovici et al.*, 1992], other geodynamic studies demonstrated that including compressibility into mantle convection models, which introduces viscous heating and depth dependence of material properties such as density, expansivity, diffusivity, and heat capacity, tends to reduce the convective vigor of the system [*Tackley*, 1996]. Of most relevance to our study are the effects that compressibility introduces in thermochemical convection, which are absent from our model. In particular, *Hansen and Yuen* [2000] have shown that the depth dependence of thermal expansivity, i.e., its decrease with depth, facilitates the preservation of a compositionally dense basal heterogeneity. Additional effects of compressibility come from the notion that different materials (e.g., subducted oceanic crust and ambient mantle) may have different bulk moduli and consequently different adiabatic density profiles. This leads to depth dependence of density contrast between these

materials and gives rise to thermochemical structures that can only be observed in compressible convection models, such as oscillating and stagnating plumes [*Samuel and Bercovici*, 2006] and metastable superplumes [*Tan and Gurnis*, 2005, 2007].

A2. Cylindrical Geometry

Different ways of constructing two-dimensional models that can reflect physical processes occurring in a more Earth-like three-dimensional sphere have been proposed [e.g., *van Keken*, 2001; *Hernlund and Tackley*, 2008]. The quantities often considered are heat flux, usually in terms of the Nusselt number (*Nu*), the characteristic flow velocity, usually in terms of the root-mean-square or surface velocity and the characteristic length-scales of thermal structures, such as distance between neighboring upwellings or downwellings. For a two-dimensional hollow-cylinder geometry (such as in our model), geometrical parameters that need to be prescribed are inner (R_i) and outer (R_o) radii. Scaling R_i and R_o directly to the radii of the outer core ($\approx$ 3486 km) and the surface of the Earth ($\approx$ 6371 km), respectively, gives $R_i = 1.2083$ and $R_o = 2.2083$, where the nondimensional depth of the mantle is chosen to be 1. *van Keken* [2001] have shown that this choice of geometry results in an overestimation of heat flux and flow velocity and that a scaling with $R_i = 0.4292$ and $R_o = 1.4292$ produces results that more closely resemble thermal convection in a sphere. The fact that increasing the curvature of the cylinder (decreasing the ratio of inner to outer radii) leads to a decrease in heat flux has been previously demonstrated in a systematic numerical study of *Jarvis* [1993]. An analogous effect of curvature on heat transport properties has also been demonstrated in models of mantle convection in three-dimensional spherical geometry [*Hosein Shahnas et al.*, 2008; *Deschamps et al.*, 2010]. However, *Hernlund and Tackley* [2008] have pointed out that using such small inner radius for cylindrical geometry as proposed by *van Keken* [2001] leads to an artificial "crowding" of thermal and compositional structures at the base of the mantle. Further, as was pointed out by *Hosein Shahnas et al.* [2008], mechanical boundary conditions (e.g., free slip or prescribed velocities) may also play a role in the resulting heat flux of a model. A similar observation was made in *van Keken and Ballentine* [1999], namely, that one cannot independently adjust model parameters such as plate velocities and heat flow.

With these limitations in mind, we choose to set the nondimensional inner and outer radii of our cylindrical domain equal to 1 and 2, respectively. It is an intermediate scaling compared to the ones studied in *van Keken* [2001]. With this choice of model parameters, including the geometrical parameters, the previously described mechanical boundary conditions (section 2.2), and the viscosity model (section 2.3), we observed that *Nu* (here measured as the nondimensional conductive surface heat flux) in our models never exceeded the value of 16. This value is on the lower end of the range suggested for the surface of the Earth (*Nu* between 14 and 23, as summarized in *van Keken and Ballentine* [1999]). Just to get an idea of how the nondimensional heat flow values obtained in our models relate to Earth, we dimensionalized the values of circumference-averaged conductive radial heat flux, measured at the top and bottom boundaries of our models, and integrated these over the spherical surface area of the Earth and CMB, respectively. Thus, in dimensional terms, the range of present-day surface heat flow values obtained in our models is 18–25 TW, which is smaller than the estimated range of convecting mantle heat flow of 35–43 TW [*Jaupart et al.*, 2007]. For further comparison, the present-day surface heat flow obtained in the "best fit" thermochemical convection model of *Nakagawa and Tackley* [2014], who used a spherical annulus geometry as described in *Hernlund and Tackley* [2008], is about 30 TW. The range of the present-day CMB heat flow values obtained in our models is 7–13 TW, which is larger than the theoretical estimates of ~2.1–3.4 TW in *Buffett* [2002], but within the range of the more recent estimates of ~5–15 TW, as summarized in *Lay et al.* [2008]. Conversely, the most successful thermochemical convection model of *Nakagawa and Tackley* [2005], who used a scaled cylindrical geometry as described in *van Keken* [2001], predicts a present-day CMB heat flow of 8.5 TW. The low surface heat flow values obtained in our models are likely due to our chosen value for the prescribed surface velocity, which is lower than the typical tectonic velocities. The high CMB heat flow in our models is partially due to the choice of geometry, which overestimates the "surface" of the hot CMB, and partially due to the absence of internal heating.

A3. Prescribed Surface Velocity

The constant in time-prescribed surface velocity in our models is an oversimplification of plate tectonics at the Earth's surface, where plate boundaries migrate, new plate boundaries get created, and old boundaries stop being active, or get extinguished altogether. Rearrangement of plate boundaries with time leads to an unsteady mantle convection pattern, which, in turn, can lead to more chaotic mantle flow and more efficient stirring of chemical heterogeneities [*Gurnis and Davies*, 1986a; *Kellogg and*

Turcotte, 1990; *Christensen*, 1989]. Thus, our chosen constant in time surface boundary conditions facilitate the segregation and preservation of dense material at the base.

A4. Internal Heating

For simplicity, we do not include internal heating into our models. One of the consequences of excluding the internal heating mode are excessively hot and buoyant thermal plumes, compared to what is expected in a more Earth-like convection. While excess buoyancy contributes to faster ascent of the plume and, thus, promotes entrainment and destruction of the compositionally dense anomaly, the hotter temperature of the plume also makes it less viscous and, thus, lowers its ability to entrain the dense material. The net effect of excessively hot plumes on entrainment is thus difficult to assess.

Further, radioactive elements are distributed heterogeneously throughout the Earth's mantle, giving rise to thermal variations that cannot be captured by our model. In particular, because radioactive elements preferentially enter the basaltic component upon mantle-melting at the surface, the OC has a higher concentration of these heat-producing elements compared to ambient mantle. Thus, a large-scale compositional anomaly made up by segregated OC, as featured in our models, experiences more internal heating than the ambient mantle. The resulting excess heat of the piles would make them less gravitationally stable, compared to the ones produced in our models.

Further, lack of internally generated heat may lead to an excessively cool mantle. However, this effect may be somewhat compensated by our choice of the two-dimensional cylindrical geometry, with the hot inner boundary that is relatively large compared to the cool outer boundary. On similar effects of model geometry on the heating mode in convection simulations, see *O'Farrell and Lowman* [2010].

A5. Stress Exponent

When the diffusion creep is the dominant deformation mechanism, the material behaves like a Newtonian fluid, and the dependence of strain rate on stress is linear, i.e., $n = 1$. When the fluid deforms predominantly by dislocation (or power law) creep, this dependence is normally approximated to be given by $n = 3$ [e.g., *Karato*, 2008]. Which values of n are appropriate in different regions of the mantle is not well constrained. Laboratory studies [e.g., *Karato et al.*, 1995; *Karato and Wu*, 1993] and inferences of mantle anisotropy structure from seismological studies [*Becker*, 2006; *Karato*, 1998] favor the dominance of dislocation creep in the shallow upper mantle, and possibly inside the D'' layer and dominance of diffusion creep in the lower mantle.

The effect of different mantle rheology models, linear or nonlinear, on the mantle flow has been studied in *Christensen*, [1983, 1984]. The general effect of nonlinear rheology has been found to reduce the viscosity variations associated with pressure dependence and temperature dependence, compared to the linear rheology case. In the same study it has been demonstrated that the nonlinear rheology can be closely imitated by a Newtonian flow with a reduced value of activation enthalpy, by a factor of 0.3–0.5. The main difference between a power law flow imitated by a Newtonian flow with a reduced enthalpy, and an actual power-law, is the tendency of the latter to concentrate the deformation into certain regions. This effect is important for incorporating self-consistent plate tectonics into mantle convection models, which may require weakening of the lithosphere in the subduction zones due to stress concentrations. However, our current model does not include this feature.

Acknowledgments

The authors thank two anonymous reviewers for detailed comments and helpful suggestions. E.M. was supported by a scholarship from the graduate research school GeoSim, which is funded by the Helmholtz association and grants from its home institutions: GFZ Potsdam, Freie Universitat Berlin and Universitat Potsdam. We would like to thank the Weierstrass Institute for Applied Analysis and Stochastics (WIAS) in Berlin, Germany, as well as the Computational Geology Laboratory at the Polish Geological Institute in Wroclaw, Poland, for the generously provided computational resources. We thank Marcin Krotkiewski at Physics of Geological Processes (PGP), University of Oslo, Norway, for the support in code development. The numerical code that was used to generate the results in this study builds on open source packages MILAMIN and MUTILS, and are available upon request from the corresponding author (E.M.). We are grateful to our colleagues from the Geodynamic Modeling section 2.5 at GFZ, Potsdam, Germany, for stimulating discussions. Especially warm thanks from E.M. to Andrey Babeyko and Alexei Petrunin for the valuable scientific advice, and not the least for the frequent pep talks, firm nudges toward writing papers, and for creating a humorous and friendly working atmosphere.

References

Becker, T. (2006), On the effect of temperature and strain-rate dependent viscosity on global mantle flow, net rotation, and plate-driving forces, *Geophys. J. Int.*, *167*(2), 943–957.

Bercovici, D., G. Schubert, and G. A. Glatzmaier (1992), Three-dimensional convection of an infinite-Prandtl-number compressible fluid in a basally heated spherical shell, *J. Fluid Mech.*, *239*, 683–719.

Blankenbach, B., et al. (1989), A benchmark comparison for mantle convection codes, *Geophys. J. Int.*, *98*(1), 23–38.

Bower, D. J., M. Gurnis, and M. Seton (2013), Lower mantle structure from paleogeographically constrained dynamic Earth models, *Geochem. Geophys. Geosyst.*, *14*, 44–63, doi:10.1029/2012GC004267.

Brandenburg, J., and P. Van Keken (2007), Deep storage of oceanic crust in a vigorously convecting mantle, *J. Geophys. Res.*, *112*, B06403, doi:10.1029/2006JB004813.

Buffett, B. A. (2002), Estimates of heat flow in the deep mantle based on the power requirements for the geodynamo, *Geophys. Res. Lett.*, *29*(12), 1256, doi:10.1029/2001GL014649.

Burke, K., B. Steinberger, T. H. Torsvik, and M. A. Smethurst (2008), Plume generation zones at the margins of large low shear velocity provinces on the core-mantle boundary, *Earth Planet. Sci. Lett.*, *265*(1), 49–60.

Christensen, U. (1983), Convection in a variable-viscosity fluid: Newtonian versus power-law rheology, *Earth Planet. Sci. Lett.*, *64*(1), 153–162.

Christensen, U. (1984), Convection with pressure-and temperature-dependent non-Newtonian rheology, *Geophys. J. R. Astron. Soc.*, *77*(2), 343–384.

Christensen, U. (1989), Mixing by time-dependent convection, *Earth Planet. Sci. Lett.*, *95*(3), 382–394.
Christensen, U., and A. Hofmann (1994), Segregation of subducted oceanic crust in the convecting mantle, *J. Geophys. Res.*, *19*(B10), 867–819.
Dabrowski, M., M. Krotkiewski, and D. Schmid (2008), MILAMIN: MATLAB-based finite element method solver for large problems, *Geochem. Geophys. Geosyst.*, *9*, Q04030, doi:10.1029/2007GC001719.
Davaille, A. (1999), Simultaneous generation of hotspots and superswells by convection in a heterogeneous planetary mantle, *Nature*, *402*(6763), 756–760.
Davaille, A., F. Girard, and M. Le Bars (2002), How to anchor hotspots in a convecting mantle?, *Earth Planet. Sci. Lett.*, *203*(2), 621–634.
Davies, G. F. (2002), Stirring geochemistry in mantle convection models with stiff plates and slabs, *Geochim. Cosmochim. Acta*, *66*(17), 3125–3142.
Deschamps, F., P. J. Tackley, and T. Nakagawa (2010), Temperature and heat flux scalings for isoviscous thermal convection in spherical geometry, *Geophys. J. Int.*, *182*(1), 137–154.
Deschamps, F., L. Cobden, and P. J. Tackley (2012), The primitive nature of large low shear-wave velocity provinces, *Earth Planet. Sci. Lett.*, *349*, 198–208.
Deubelbeiss, Y., and B. Kaus (2008), Comparison of Eulerian and Lagrangian numerical techniques for the Stokes equations in the presence of strongly varying viscosity, *Phys. Earth Planet. Inter.*, *171*(1–4), 92–111.
Duretz, T., D. May, T. Gerya, and P. Tackley (2011), Discretization errors and free surface stabilization in the finite difference and marker-in-cell method for applied geodynamics: A numerical study, *Geochem. Geophys. Geosyst.*, *12*, Q07004, doi:10.1029/2011GC003567.
Dziewonski, A., and D. Anderson (1981), Preliminary reference Earth model* 1, *Phys. Earth Planet. Inter.*, *25*(4), 297–356.
Dziewonski, A., V. Lekic, and B. Romanowicz (2010), Mantle anchor structure: An argument for bottom up tectonics, *Earth Planet. Sci. Lett.*, *299*, 69–79.
Garnero, E., and A. McNamara (2008), Structure and dynamics of Earth's lower mantle, *Science*, *320*(5876), 626–628.
Gerya, T., and D. Yuen (2003), Characteristics-based marker-in-cell method with conservative finite-differences schemes for modeling geological flows with strongly variable transport properties, *Phys. Earth Planet. Inter.*, *140*(4), 293–318.
Gonnermann, H. M., A. M. Jellinek, M. A. Richards, and M. Manga (2004), Modulation of mantle plumes and heat flow at the core mantle boundary by plate-scale flow: Results from laboratory experiments, *Earth Planet. Sci. Lett.*, *226*(1), 53–67.
Gurnis, M. (1986), The effects of chemical density differences on convective mixing in the Earth's mantle, *J. Geophys. Res.*, *91*(B11), 11,407–11,419.
Gurnis, M., and G. F. Davies (1986a), Mixing in numerical models of mantle convection incorporating plate kinematics, *J. Geophys. Res.*, *91*(B6), 6375–6395.
Gurnis, M., and G. F. Davies (1986b), The effect of depth-dependent viscosity on convective mixing in the mantle and the possible survival of primitive mantle, *Geophys. Res. Lett.*, *13*(6), 541–544.
Hansen, U., and D. Yuen (2000), Extended-Boussinesq thermal–chemical convection with moving heat sources and variable viscosity, *Earth Planet. Sci. Lett.*, *176*(3), 401–411.
Hayden, L., and E. Watson (2007), A diffusion mechanism for core–mantle interaction, *Nature*, *450*(7170), 709–711.
He, Y., and L. Wen (2009), Structural features and shear-velocity structure of the 'Pacific anomaly', *J. Geophys. Res.*, *114*, B02309, doi:10.1029/2008JB005814.
Hernlund, J. W., and C. Houser (2008), On the statistical distribution of seismic velocities in Earth's deep mantle, *Earth Planet. Sci. Lett.*, *265*(3), 423–437.
Hernlund, J. W., and P. J. Tackley (2008), Modeling mantle convection in the spherical annulus, *Phys. Earth Planet. Inter.*, *171*(1), 48–54.
Hirose, K., N. Takafuji, N. Sata, and Y. Ohishi (2005), Phase transition and density of subducted MORB crust in the lower mantle, *Earth Planet. Sci. Lett.*, *237*(1), 239–251.
Hofmann, A. W., and W. M. White (1982), Mantle plumes from ancient oceanic crust, *Earth Planet. Sci. Lett.*, *57*(2), 421–436.
Hosein Shahnas, M., J. P. Lowman, G. T. Jarvis, and H.-P. Bunge (2008), Convection in a spherical shell heated by an isothermal core and internal sources: Implications for the thermal state of planetary mantles, *Phys. Earth Planet. Inter.*, *168*(1), 6–15.
Huang, J., and G. F. Davies (2007), Stirring in three-dimensional mantle convection models and implications for geochemistry: 2. Heavy tracers, *Geochem. Geophys. Geosyst.*, *8*, Q07004, doi:10.1029/2007GC001621.
Ishii, M., and J. Tromp (1999), Normal-mode and free-air gravity constraints on lateral variations in velocity and density of Earth's mantle, *Science*, *285*(5431), 1231–1236.
Jarvis, G. T. (1993), Effects of curvature on two-dimensional models of mantle convection: Cylindrical polar coordinates, *J. Geophys. Res.*, *98*(B3), 4477–4485.
Jaupart, C., S. Labrosse, and J. Mareschal (2007), Temperatures, heat and energy in the mantle of the Earth, in *Treatise on Geophysics: Mantle Dynamics*, vol. 7, edited by D. Bercovici and G. Schubert, pp. 253–303, Elsevier, Amsterdam.
Karato, S. (1998), Seismic anisotropy in the deep mantle, boundary layers and the geometry of mantle convection, *Pure Appl. Geophys.*, *151*(2–4), 565–587.
Karato, S. (2008), *Deformation of Earth Materials: An Introduction to the Rheology of Solid Earth*, Cambridge Univ. Press, London.
Karato, S., and P. Wu (1993), Rheology of the upper mantle: A synthesis, *Science*, *260*(5109), 771–778.
Karato, S.-i., S. Zhang, and H. -R. Wenk (1995), Superplasticity in Earth's lower mantle: Evidence from seismic anisotropy and rock physics, *Science*, *270*(5235), 458–461.
Kellogg, L., and D. Turcotte (1990), Mixing and the distribution of heterogeneities in a chaotically convecting mantle, *J. Geophys. Res.*, *95*(B1), 421–432.
Kellogg, L. H., B. H. Hager, and R. D. van der Hilst (1999), Compositional stratification in the deep mantle, *Science*, *283*(5409), 1881–1884.
Kobayashi, K., R. Tanaka, T. Moriguti, K. Shimizu, and E. Nakamura (2004), Lithium, boron, and lead isotope systematics of glass inclusions in olivines from Hawaiian lavas: Evidence for recycled components in the hawaiian plume, *Chem. Geol.*, *212*(1), 143–161.
Krotkiewski, M. (2013), MUTILS — A set of efficient modeling tools for multi-core CPUs implemented in MEX. Abstracts EGU2013-7877 paper presented at EGU General Assembly Conference 2013, Vienna, 7–12 April.
Kumagai, I., A. Davaille, and K. Kurita (2007), On the fate of thermally buoyant mantle plumes at density interfaces, *Earth Planet. Sci. Lett.*, *254*(1), 180–193.
Labrosse, S., J. Hernlund, and N. Coltice (2007), A crystallizing dense magma ocean at the base of the Earth's mantle, *Nature*, *450*(7171), 866–869.
Lay, T., J. Hernlund, and B. A. Buffett (2008), Core-mantle boundary heat flow, *Nat. Geosci.*, *1*(1), 25–32.
Le Bars, M., and A. Davaille (2004), Whole layer convection in a heterogeneous planetary mantle, *J. Geophys. Res.*, *109*, B03403, doi:10.1029/2003JB002617.

Lee, C., P. Luffi, T. Höink, J. Li, R. Dasgupta, and J. Hernlund (2010), Upside-down differentiation and generation of a 'primordial' lower mantle, *Nature*, *463*(7283), 930–933.
LeVeque, R. J. (2002), *Finite Volume Methods for Hyperbolic Problems*, vol. 31, Cambridge Univ. Press, Cambridge, U. K.
Li, M., and A. K. McNamara (2013), The difficulty for subducted oceanic crust to accumulate at the Earth's core-mantle boundary, *J. Geophys. Res. Solid Earth*, *118*, 1807–1816, doi:10.1002/jgrb.50156.
Li, Y., F. Deschamps, and P. J. Tackley (2014), The stability and structure of primordial reservoirs in the lower mantle: Insights from models of thermochemical convection in three-dimensional spherical geometry, *Geophys. J. Int.*, *199*(2), 914–930.
Lin, S. -C., and P. E. van Keken (2006), Dynamics of thermochemical plumes: 1. Plume formation and entrainment of a dense layer, *Geochem. Geophys. Geosyst.*, *7*, Q02006, doi:10.1029/2005GC001071.
Masters, G., G. Laske, H. Bolton, and A. Dziewonski (2000), The relative behavior of shear velocity, bulk sound speed, and compressional velocity in the mantle: Implications for chemical and thermal structure, in *Earth's Deep Interior: Mineral Physics and Tomography From the Atomic to the Global Scale*, edited by S.-I. Karato et al., pp. 63–87, AGU, Washington, D. C., doi:10.1029/GM117p0063.
Moresi, L., S. Zhong, and M. Gurnis (1996), The accuracy of finite element solutions of Stokes's flow with strongly varying viscosity, *Phys. Earth Planet. Inter.*, *97*(1), 83–94.
Mosca, I., L. Cobden, A. Deuss, J. Ritsema, and J. Trampert (2012), Seismic and mineralogical structures of the lower mantle from probabilistic tomography, *J. Geophys. Res.*, *117*, B06304, doi:10.1029/2011JB008851.
Nakagawa, T., and P. J. Tackley (2005), Deep mantle heat flow and thermal evolution of the Earth's core in thermochemical multiphase models of mantle convection, *Geochem. Geophys. Geosyst.*, *6*, Q08003, doi:10.1029/2005GC000967.
Nakagawa, T., and P. J. Tackley (2014), Influence of combined primordial layering and recycled MORB on the coupled thermal evolution of Earth's mantle and core, *Geochem. Geophys. Geosyst.*, *15*, 619–633, doi:10.1002/2013GC005128.
Nakagawa, T., P. Tackley, F. Deschamps, and J. Connolly (2010), The influence of MORB and harzburgite composition on thermo-chemical mantle convection in a 3-D spherical shell with self-consistently calculated mineral physics, *Earth Planet. Sci. Lett.*, *296*(3), 403–412.
Ni, S., and D. V. Helmberger (2003), Seismological constraints on the South African superplume; could be the oldest distinct structure on Earth, *Earth Planet. Sci. Lett.*, *206*(1), 119–131.
Ni, S., E. Tan, M. Gurnis, and D. Helmberger (2002), Sharp sides to the African superplume, *Science*, *296*(5574), 1850–1852.
Nutman, A. P. (2006), Antiquity of the oceans and continents, *Elements*, *2*(4), 223–227.
O'Farrell, K. A., and J. P. Lowman (2010), Emulating the thermal structure of spherical shell convection in plane-layer geometry mantle convection models, *Phys. Earth Planet. Inter.*, *182*(1), 73–84.
Olson, P., and C. Kincaid (1991), Experiments on the interaction of thermal convection and compositional layering at the base of the mantle, *J. Geophys. Res.*, *96*(B3), 4347–4354.
Ricolleau, A., J. -P. Perrillat, G. Fiquet, I. Daniel, J. Matas, A. Addad, N. Menguy, H. Cardon, M. Mezouar, and N. Guignot (2010), Phase relations and equation of state of a natural MORB: Implications for the density profile of subducted oceanic crust in the Earth's lower mantle, *J. Geophys. Res.*, *115*, B08202, doi:10.1029/2009JB006709.
Ritsema, J., A. Deuss, H. Van Heijst, and J. Woodhouse (2011), S40RTS: A degree-40 shear-velocity model for the mantle from new Rayleigh wave dispersion, teleseismic traveltime and normal-mode splitting function measurements, *Geophys. J. Int.*, *184*(3), 1223–1236.
Samuel, H., and D. Bercovici (2006), Oscillating and stagnating plumes in the Earth's lower mantle, *Earth Planet. Sci. Lett.*, *248*(1), 90–105.
Schubert, G., D. Turcotte, and P. Olson (2001), Mantle convection in the Earth and planets.
Shewchuk, J. (1996), Triangle: Engineering a 2D quality mesh generator and Delaunay triangulator, in *Applied Computational Geometry Towards Geometric Engineering*, edited by M. C. Lin and D. Manocha, pp. 203–222, Springer, Berlin.
Shirey, S. B., and S. H. Richardson (2011), Start of the Wilson Cycle at 3 Ga shown by diamonds from subcontinental mantle, *Science*, *333*(6041), 434–436.
Sleep, N. (1988), Gradual entrainment of a chemical layer at the base of the mantle by overlying convection, *Geophys. J.*, *95*(3), 437–447.
Sobolev, A. V., A. W. Hofmann, S. V. Sobolev, and I. K. Nikogosian (2005), An olivine-free mantle source of Hawaiian shield basalts, *Nature*, *434*(7033), 590–597.
Sobolev, A. V., et al. (2007), The amount of recycled crust in sources of mantle-derived melts, *Science*, *316*(5823), 412–417.
Sobolev, S., A. Sobolev, D. Kuzmin, N. Krivolutskaya, A. Petrunin, N. Arndt, V. Radko, and Y. Vasiliev (2011), Linking mantle plumes, large igneous provinces and environmental catastrophes, *Nature*, *477*(7364), 312–316.
Solomatov, V., P. Olson, and D. Stevenson (1993), Entrainment from a bed of particles by thermal convection, *Earth Planet. Sci. Lett.*, *120*(3), 387–393.
Steinberger, B., and A. Calderwood (2006), Models of large-scale viscous flow in the Earth's mantle with constraints from mineral physics and surface observations, *Geophys. J. Int.*, *167*(3), 1461–1481.
Steinberger, B., and R. Holme (2008), Mantle flow models with core-mantle boundary constraints and chemical heterogeneities in the lowermost mantle, *J. geophys. Res*, *113*, B05403, doi:10.1029/2007JB005080.
Stixrude, L., and C. Lithgow-Bertelloni (2012), Geophysics of chemical heterogeneity in the mantle, *Annu. Rev. Earth Planet. Sci.*, *40*, 569–595.
Tackley, P. (1996), Effects of strongly variable viscosity on three-dimensional compressible convection in planetary mantles, *J. Geophys. Res.*, *101*(B2), 3311–3332.
Tackley, P. (2002), Strong heterogeneity caused by deep mantle layering, *Geochem. Geophys. Geosyst*, *3*(4), 1024.
Tackley, P. (2011), Living dead slabs in 3-D: The dynamics of compositionally-stratified slabs entering a 'slab graveyard' above the core-mantle boundary, *Phys. Earth Planet. Inter.*, *188*(3–4), 150–162.
Tackley, P., and S. King (2003), Testing the tracer ratio method for modeling active compositional fields in mantle convection simulations, *Geochem. Geophys. Geosyst.*, *4*(4), 8302, doi:10.1029/2001GC000214.
Tackley, P. J. (2012), Dynamics and evolution of the deep mantle resulting from thermal, chemical, phase and melting effects, *Earth Sci. Rev.*, *110*(1), 1–25.
Tan, E., and M. Gurnis (2005), Metastable superplumes and mantle compressibility, *Geophys. Res. Lett*, *32*, L20307, doi:10.1029/2005GL024190.
Tan, E., and M. Gurnis (2007), Compressible thermochemical convection and application to lower mantle structures, *J. Geophys. Res.*, *112*, B06304, doi:10.1029/2006JB004505.
Tan, E., W. Leng, S. Zhong, and M. Gurnis (2011), On the location of plumes and lateral movement of thermochemical structures with high bulk modulus in the 3-D compressible mantle, *Geochem. Geophys. Geosyst.*, *12*, Q07005, doi:10.1029/2011GC003665.
Torsvik, T., M. Smethurst, K. Burke, and B. Steinberger (2006), Large igneous provinces generated from the margins of the large low-velocity provinces in the deep mantle, *Geophys. J. Int.*, *167*(3), 1447–1460.
Trampert, J., F. Deschamps, J. Resovsky, and D. Yuen (2004), Probabilistic tomography maps chemical heterogeneities throughout the lower mantle, *Science*, *306*(5697), 853–856.

Tsuchiya, T. (2011), Elasticity of subducted basaltic crust at the lower mantle pressures: Insights on the nature of deep mantle heterogeneity, *Phys. Earth Planet. Inter.*, *188*(3), 142–149.

Van der Hilst, R., S. Widiyantoro, K. Creager, and T. McSweeney (1998), Deep subduction and aspherical variations in P-wavespeed at the base of Earth's mantle, in *The Core-Mantle Boundary Region, Geodyn. Ser.*, vol. 28, edited by M. Gurnis et al., pp. 5–20, AGU, Washington, D. C.

van Keken, P. (2001), Cylindrical scaling for dynamical cooling models of the Earth, *Phys. Earth Planet. Inter.*, *124*(1), 119–130.

van Keken, P., and C. Ballentine (1999), Dynamical models of mantle volatile evolution and the role of phase transitions and temperature-dependent rheology, *J. Geophys. Res.*, *104*(B4), 7137–7151.

Van Keken, P., S. King, H. Schmeling, U. Christensen, D. Neumeister, and M. Doin (1997), A comparison of methods for the modeling of thermochemical convection, *J. Geophys. Res.*, *102*, 22–22.

Wang, Y., and L. Wen (2007), Geometry and P and S velocity structure of the "African anomaly", *J. Geophys. Res.*, *112*, B05313, doi:10.1029/2006JB004483.

Xie, S., and P. J. Tackley (2004), Evolution of U-Pb and Sm-Nd systems in numerical models of mantle convection and plate tectonics, *J. Geophys. Res.*, *109*, B11204, doi:10.1029/2004JB003176.

Zhong, S., and B. Hager (2003), Entrainment of a dense layer by thermal plumes, *Geophys. J. Int.*, *154*(3), 666–676.